LBNL-46001

ERNEST ORLANDO LAWRENCE
BERKELEY NATIONAL LABORATORY

Experimental and Theoretical Studies of Picosecond Laser Interactions with Electronic Materials—Laser Ablation

Samuel S. Mao

Environmental Energy Technologies Division

May 2000

Ph.D. Thesis

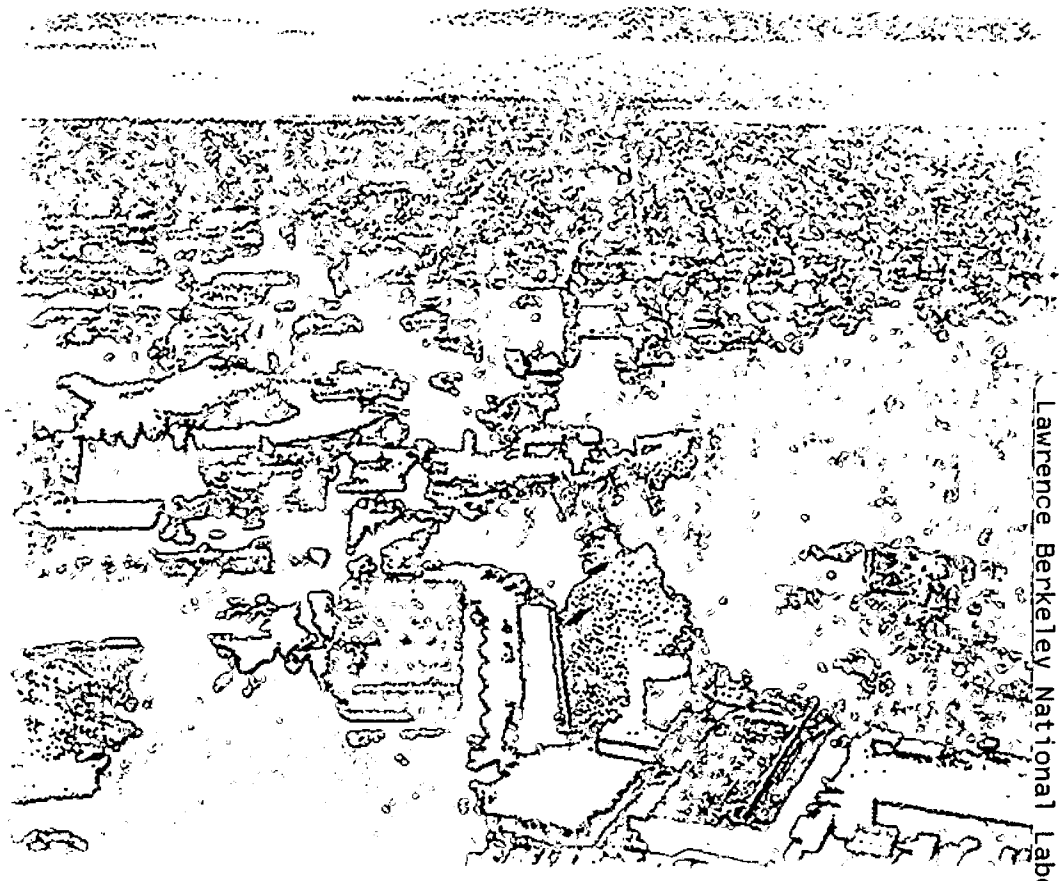

DISCLAIMER

LBNL-46001

Experimental and Theoretical Studies of Picosecond Laser Interactions with Electronic Materials—Laser Ablation

Samuel S. Mao
Ph.D. Thesis

Department of Mechanical Engineering
University of California, Berkeley

and

Environmental Energy Technologies Division
Advanced Energy Technologies Department
Ernest Orlando Lawrence Berkeley National Laboratory
University of California
Berkeley, CA 94720

May 2000

This work was supported by the Director, Office of Science, Office of Basic Energy Sciences, of the U.S. Department of Energy under Contract No. DE-AC03-76SF00098.

Experimental and Theoretical Studies of Picosecond Laser Interactions with Electronic Materials – Laser Ablation

by

Samuel S. Mao

B.Sc. (Nanjing University, China) 1990

M.Sc. (University of Newfoundland, Canada) 1996

A dissertation submitted in partial satisfaction of the

requirements for the degree of

Doctor of Philosophy

in

Engineering - Mechanical Engineering

in the

GRADUATE DIVISION

of the

UNIVERSITY OF CALIFORNIA, BERKELEY

Committee in charge:

Professor Ralph Greif, Chair

Professor Costas P. Grigoropoulos

Professor Per Peterson

Spring 2000

Experimental and Theoretical Studies of Picosecond Laser Interactions with Electronic Materials—Laser Ablation

by

Samuel S. Mao

Abstract

Experimental and Theoretical Studies of Picosecond Laser Interactions with Electronic Materials – Laser Ablation

Samuel S. Mao

Doctor of Philosophy in Engineering

University of California at Berkeley

Professor Ralph Greif, Chair

Lasers having picosecond and shorter pulse duration are receiving much attention due to their capabilities for direct-write micromachining on many materials with minimal substrate damage. Substantial progress has been made in the understanding of laser ablation processes, particularly the creation of plasmas that often shield the target and reduce the material processing efficiency at nanosecond time scales. However, a considerable challenge that still remains is the understanding of the underlying mechanisms during picosecond laser interactions with electronic solids.

In this work, we first study picosecond laser-induced electron emission from semiconductor surfaces. A theoretical model was set up based on carrier transport inside the semiconductor material during picosecond laser-semiconductor interactions. We demonstrate that nonequilibrium carrier dynamics plays a significant role for picosecond, as well as short nanosecond, laser induced electron emission from semiconductors. Photoelectric effect is found to be responsible for

electron emission at low incident laser fluences, whereas thermionic emission is dominant at higher fluences.

We have also performed experimental and theoretical studies on the formation and subsequent evolution of plasmas during laser-metal interactions at the picosecond time scale. Using picosecond time-resolved shadowgrams and interferograms, a novel type of plasma is observed, which has an electron density on the order of 10^{20} cm^{-3}. The origin of this picosecond plasma is attributed to gas breakdown, which is caused by laser-induced electron emission from the target surface. After the laser pulse is completed, the longitudinal expansion of the plasma is suppressed. This suppression is found to result from an electric field above the target that prevents, after laser irradiation, further movement of the electrons inside the plasma.

Measurements of lateral plasma expansion indicate that the picosecond plasma may absorb substantial amount of incident laser energy during laser irradiation. This result is consistent with the measurements of laser ablation efficiency, which levels off when the laser fluence exceeds a certain threshold. The information provided in this work would be essential for precise control of laser energy coupling with materials, particularly for machining at microscale depth.

Experimental and Theoretical Studies of Picosecond Laser Interactions with Electronic Materials – Laser Ablation

List of Figures

ACKNOWLEDEMENTS

It is my great pleasure to express my sincere appreciation to my research supervisor, Professor Ralph Greif, for his valuable advice and encouragement on every aspect of my study and research at Berkeley. I am indebted to Dr. Richard E. Russo, the leader of the Advanced Laser Technologies group at Lawrence Berkeley National Laboratory, for his insight and support throughout my research. I am also grateful to Dr. Xianglei Mao of the Advanced Laser Technologies group, for many stimulating discussions and generous assistance at all stages of the present work. Last but not the least, I would like to extend my gratitude to Professor Costas Grigoropoulos and Professor Per Peterson, for their strong interest of the subject and careful review of this dissertation.

Chapter 1

INTRODUCTION

1.1 Laser ablation

Laser ablation (Miller and Haglund, 1998; von Allmen and Blatter, 1995) refers to mass removal from target surface by coupling substantial laser energies into the target material. It is a complex, collective process involving a tangle of questions regarding photon-matter interactions at high photon flux. A schematic illustration of laser ablation is shown in figure 1. Despite its increasing number of applications (Russo et al., 1998), many fundamental aspects of laser ablation are still unknown.

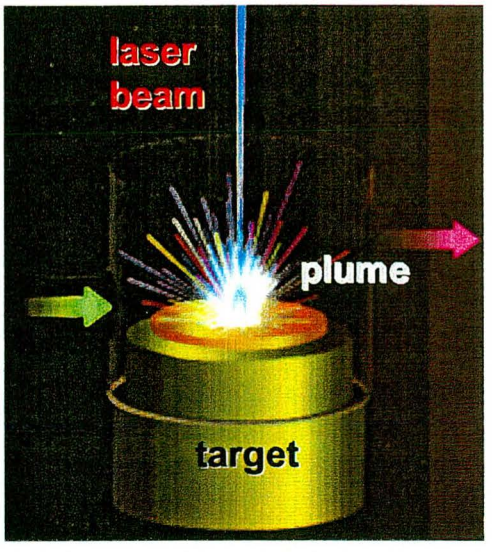

Figure 1.1. A schematic illustration of laser ablation.

Of primary interest to this study is the ablation process using picosecond solid state Nd:YAG lasers (Yariv, 1997). In such lasers, Neodymium atoms are implanted in host yttrium-aluminum-garnet (YAG) crystals, and the laser emits in the near infrared at 1064 nm wavelength. This type of solid laser has been used in a variety of applications requiring high photon fluxes (laser-induced nuclear fusion is one example).

Contemporary pulse compression technologies allow the duration of a laser beam to vary anywhere from a continuous beam (CW) to pulses as short as 6 femtoseconds (Yariv, 1997). The availability of different pulse duration, in conjunction with variable output energies and wavelength contributes to the versatility of solid-state lasers. Figure 1.2 shows the time scale from 1 femtosecond to 1 second on a time axis.

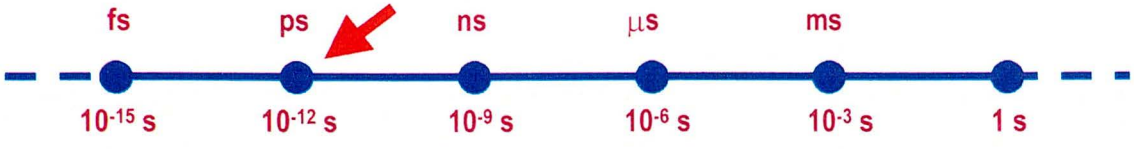

Figure 1.2. An illustration of time scales from one femtosecond to one second.

The potential of laser ablation for practical applications was realized in the 1980's after the successful demonstration of the laser-assisted fabrication of newly discovered high critical temperature superconductor films (Dijkkamp et al., 1987; Wu et al., 1987). Laser ablation has the advantage over traditional methods of thin film deposition of less restrictive with respect to materials. Not limited to depositing metal and semiconductor films, laser ablation is a viable technique for

high quality oxide films, for example, as well as many films that cannot be easily made using conventional methods (Lowndes, et al., 1996). Most recently, laser ablation has been demonstrated to be capable of synthesizing nanoscale materials (Morales and Lieber, 1996; Odom et al., 1998; Geohegan et al., 1998), which may have potential applications for miniaturization of electronic circuits.

Other areas of laser ablation applications include laser-based surgery procedures (Lin et al., 1999), laser ablation chemical analysis (Russo, 1995), and pulsed X-ray generation (Murnane et al., 1991). Of particular interest is the capability of ultrafast laser micro-machining (Craig, 1998). In addition to its versatility, i.e., pulsed lasers can be used to machine virtually every solid material, laser micro-machining has the advantage of direct-write, and three-dimensional capabilities. Figure 1.3a shows an example of a complex structure machined by the laser beam (Kovacs et al., 1998), and figure 1.3b is a three-dimensional object made by ultrafast laser micro-machining (Craig, 1998).

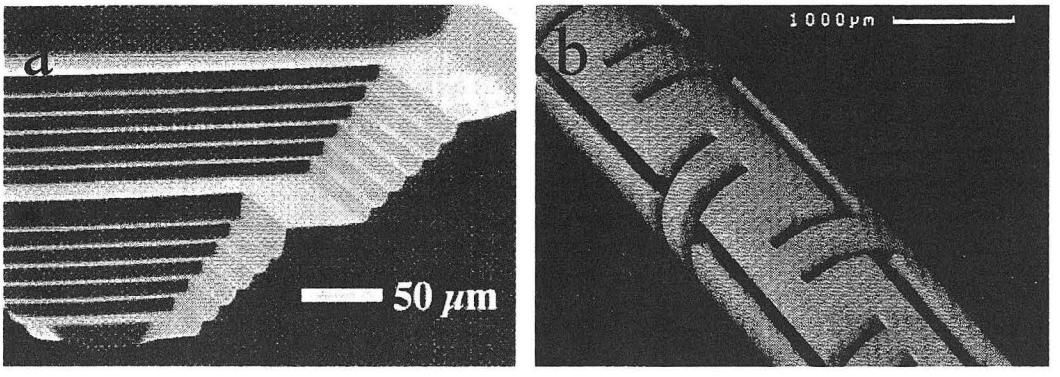

Figure 1.3. Examples of complex structures fabricated by pulsed laser micro-machining.

The microscopic mechanisms underlying the laser ablation process are quite complex. Most previous investigations have focused on laser ablation at nanosecond and longer time scales (Ho et al., 1995; Callies et al., 1995). Since the characteristic time (relaxation time) for energy exchange between electrons and material lattice is on the order of picoseconds (Kittel, 1996), thermal equilibrium has been established in nanoseconds after the ablation laser pulse is completed, and the conventional thermal model based on heat conduction equation,

$$\rho c_p \frac{\partial T}{\partial t} = -\nabla \cdot q + W_L$$

can be applied to such cases (Incropera and DeWitt, 1996). In the above equation, ρ is the density of the target material, c_p is specific heat, T is temperature (for both electrons and lattice in equilibrium), q is heat flux and W_L is energy source from the laser pulse.

For sub-nanosecond laser pulse interaction with materials, the situation is more complicated. Because the time scale of the laser ablation process is comparable to or even shorter than the electron-lattice energy relaxation time (picoseconds), the approximation that electrons have the same temperature as the material lattice is no longer valid. Previous investigations of picosecond laser-material interactions were mostly concentrated on low power laser heating of metal targets (Qiu and Tien, 1993). Picosecond laser interactions with semiconductors and high power laser interaction with solids at the picosecond time scale are not well understood.

1.2 Scope of the present work

Aimed at advancing the knowledge of picosecond laser ablation, in particular for its rapidly evolving applications to micro-machining, for instance, we performed experimental and theoretical investigations of picosecond laser induced mass removal from metal and semiconductor surfaces in a gas environment. We found a novel type of high electron density plasma that forms during the picosecond laser pulse. This plasma is responsible for the measured reduction of mass removal or ablation efficiency in the laser fluence range of the present research.

The dissertation is organized as follows. Chapter 2 presents an energy transport theory on the picosecond laser interaction with semiconductor materials. The emphasis is placed on electron emission induced by low power, picosecond laser pulses. Laser-induced electron emission serves as the first step towards substantial mass removal by high power laser pulses.

Chapter 3 discusses picosecond time resolved shadowgraphy and interferometry experiments for laser-induced plasma formation above the target surface. In contrast to a plume of vaporized target material formed during nanosecond laser ablation of solids, for which an extensive literature exists (Chen et al., 1995; Anisimov et al., 1996; Ho et al., 1995; Callies et al., 1995), a novel type of picosecond plasma is reported. Measurements are focused on the initiation and the characteristics of the plasma generated by picosecond laser ablation of copper in air.

In chapter 4, a theoretical model is established to describe the novel picosecond laser ablation plasma. Based on a two-fluid description of laser plasmas (Kruer, 1988; Hora, 1991), we include transport of particles, their momentum, and their energy in our model. A unique boundary condition is implemented in the simulation, i.e., we allow picosecond laser induced surface electron emission to provide seed electrons for the initiation of the plasma in a gas environment.

The dynamics of the picosecond laser ablation plasma is discussed in chapter 5. For longitudinal plasma movement along the direction of the laser axis, both experimental and theoretical results indicate a suppressed expansion after the picosecond laser pulse. The cause of the suppression is discussed along with a simulation that results in support of the theory. In the lateral or radial direction, experimental measurements obey a power-law relation for the time-dependent plasma expansion radius. The experimental data are compared with the similarity theory of a two-dimensional blast wave (Sedov, 1959), and the extent of the attenuation of the picosecond laser beam by the plasma is calculated. In addition, experiments are performed to determine the laser ablation efficiency by looking at the depth of the ablation craters produced by single picosecond laser pulses. The change in the ablation efficiency is correlated with the formation of the picosecond laser ablation plasma, which acts to shield the target.

The conclusions of the present work and a recommendation of future research are provided in chapter 6.

Chapter 2

ENERGY TRANSPORT DURING PICOSECOND LASER-SOLID INTERACTIONS

2.1 Introduction

Due to their important technical applications, for example, pulsed laser deposition and laser ablation chemical analysis, ultrafast processes accompanying pulsed laser-material interactions have been the subject of much interest (Fogarassy and Lazare, 1992; Miller, 1994; Russo and Mao, 1998). An important parameter in laser-material interactions is the characteristic time for electrons and lattice to reach thermal equilibrium. This is the so-called relaxation time that is on the order of a fraction of a picosecond. For slow laser-material interaction processes with time scales much larger than this time, the deposition of laser energy can be viewed as being instantaneous; the energy transport can be described by the Fourier conduction model. However, for picosecond and shorter laser pulses, the Fourier model is no longer valid because the electrons and the material lattice do not attain thermal equilibrium on the picosecond time scale.

In this chapter, the ultrafast energy transport processes during laser-metal and laser-semiconductor interactions are studied theoretically, followed by an investigation of surface electron emission as a result of picosecond laser material interactions.

2.2 Picosecond laser-metal interactions

The heat transfer mechanisms during ultrafast laser heating of metals have been studied for many years. Among the early investigations of picosecond laser-material interactions, Anisimov and co-workers (Anisimov et al., 1974) proposed a phenomenological two-temperature model to describe the electron and lattice energy exchange during laser irradiation of metals. Starting from the Boltzmann transport equations for electrons and lattice phonons, the two-temperature model has been reproduced by Qiu and Tien (Qiu and Tien, 1993).

The two basic steps that are involved in the laser-metal interactions include the deposition of laser energy on the metal target manifested in the energy of the electrons, and the energy exchange between electrons and the material lattice atoms (Kittel, 1996). The conservation equations for electron energy ε_e and lattice energy ε_l of the target metal can be expressed as

$$\frac{\partial \varepsilon_e}{\partial t} = -\nabla \cdot q_e + W_L - U_{e-l}$$

$$\frac{\partial \varepsilon_l}{\partial t} = -\nabla \cdot q_l + U_{e-l}$$

where q_e and q_l are heat fluxes for the electrons and the lattice, respectively, W_L is the energy source for the electrons due to the picosecond laser irradiation, and $U_{e\text{-}l}$ is the energy exchange between the electrons and material lattice. Using a relaxation time, τ_e, and assuming the electrons and the lattice are at the different temperature, T_e and T_l, respectively, $U_{e\text{-}l}$ is expressed as

$$U_{e-l} = c_e \frac{T_e - T_l}{\tau_e}$$

where c_e is the electron heat capacity. A list of values of τ_e has been provided by Qiu and Tien (Qiu and Tien, 1993); for example, for copper, $\tau_e = 0.6$ ps.

Using the above energy balance equations, the spatial and temporal variations of the electron and lattice temperature have been obtained for low incident laser fluences (Qiu ane Tien, 1993). At high laser fluences, previous calculations generally did not consider target melting. It is not clear to what degree the target melting would influence the calculation.

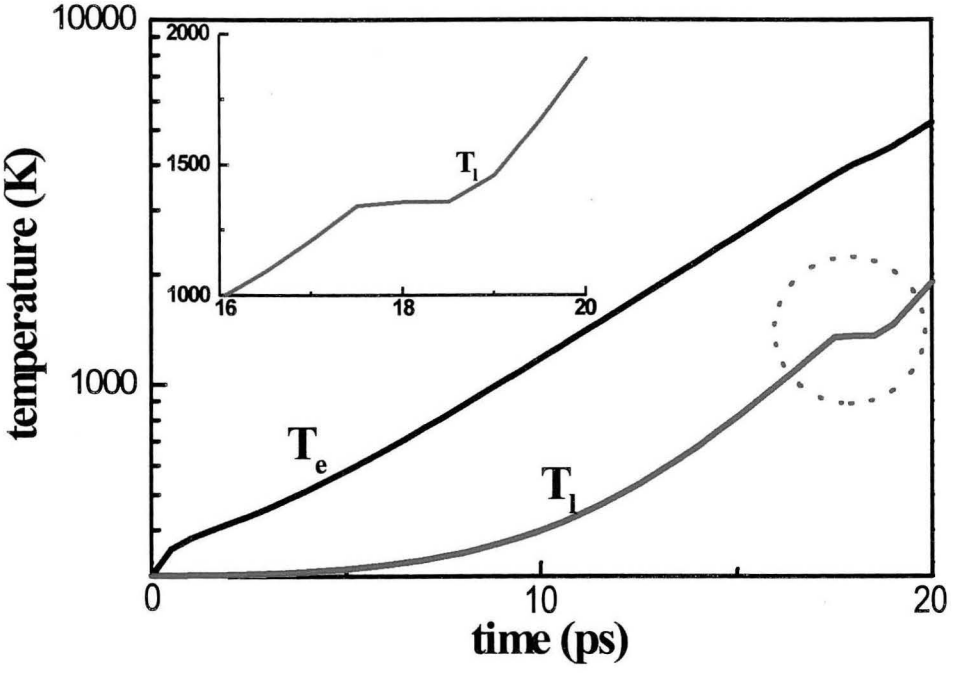

Figure 2.1. Surface electron and lattice temperature (T_e and T_l) due to a high power picosecond laser irradiation of a Cu target.

We have calculated surface electron and lattice temperatures at high laser fluences. Phase change due to target melting was incorporated into the simulation. Figure 2.1 shows the results of the calculation for 1064 nm laser irradiation of a Cu target. Starting at $t = 0$, the laser beam is assumed at the leading (rising) stage of a 35 ps (FWHM) Gaussian pulse (the peak fluence of the laser beam, 300 J/cm^2, was set at 60 ps). From figure 2.1, the target surface remains at its melting temperature for less than two picoseconds. This result implies that, unless we are dealing with a temperature range near the melting point, target melting may be neglected for simulating high power laser-interactions with metal targets.

2.3 Picosecond laser-semiconductor interactions

For ultrafast laser-semiconductor interactions, the situation is more complex than for metals, because the number of free electrons may vary with time and space. The electron temperature at the target surface, as well as within the semiconductor, is governed by transport processes associated with the evolution of hot carriers, generated by the absorption of photons from the laser pulse. In this section, we are primarily interested in 532 nm laser irradiation of an intrinsic silicon target (or slightly doped material for which the intrinsic properties dominate).

The absorption of laser radiation by silicon leads to the creation of a nonequilibrium carrier density N, as well as elevated carrier and lattice temperatures, T_e and T_l, respectively (Alfano, 1984). Here the assumption is made

that the temperatures T_e and T_l alone may describe the carriers (electrons and holes) and lattice. This is based on the consideration that for times smaller than 0.1 ps, carrier-carrier collisions result in a quasi-equilibrium distribution with a single electron and hole temperature T_e. For a typical carrier-phonon relaxation time scale of a fraction of a picosecond, hot carriers attempt to reach thermal equilibrium with the lattice by interacting with phonons (lattice oscillation modes). Therefore, the population of phonons increases due to energy exchange between the carriers and the lattice, and at times of about 10 ps, the phonons attempt to thermalize with other lattice modes, resulting in a near-equilibrium phonon state at temperature T_l (van Driel 1987).

Since the photon energy of the 532 nm laser pulse is larger than the bandgap energy E_g of silicon (E_g = 1.12 eV at 300 K), the dominant absorption mechanism is single-photon inter-band absorption that creates electron-hole pairs. Two-photon inter-band absorption and free carrier absorption can be neglected for the 532 nm laser irradiation (but cannot be neglected for infrared pulses.) In addition to absorption, electrons and holes attempt to achieve particle number equilibrium by recombination and impact ionization. Auger recombination is the dominant recombination process that transfers energy to a third carrier after two carriers recombine. Impact ionization is the inverse process of Auger recombination, an energetic carrier creates an electron-hole pair while loses its energy (Alfano, 1984).

The evolution of N, T_e and T_l in bulk silicon after pulsed laser excitation can be determined based on the coupled transport equations in the relaxation-time approximation. Transport is characterized by the balance equations for carrier density, carrier energy ε_p, and for lattice energy ε_l inside the semiconductor (Lundstrom, 1990):

$$\frac{\partial N}{\partial t} = -\nabla \cdot J_p + G_p - R_p$$
$$\frac{\partial \varepsilon_p}{\partial t} = -\nabla \cdot q_p + W_L - U_{p-l}$$
$$\frac{\partial \varepsilon_l}{\partial t} = -\nabla \cdot q_l + U_{p-l}$$

where G_p and R_p are carrier generation and recombination rates, J_p, q_p and q_l are carrier particle current, carrier energy flow and lattice heat flow, and W_L and U_{p-l} are carrier energy source and loss, respectively.

The carrier energy flow q_p and the lattice heat flow q_l can be written as,

$$q_p = -(\kappa_e + \kappa_h)\nabla T_e + (E_g + 3k_B T_e)J_p$$
$$q_l = -\kappa_l \nabla T_l$$

where κ_e, κ_h and κ_l are the electron, hole, and lattice thermal conductivity, respectively. The carrier energy loss U_{p-l} in the balance equations is given by relaxation-time approximation,

$$U_{p-l} = c_p \frac{T_e - T_l}{\tau_p}$$

where c_p is the carrier specific heat and τ_p is the carrier relaxation time. The expressions for G_p, R_p, and W_L are provided by Mao et al. (1998).

The above coupled transport equations can be solved for the spatial and temporal dependent carrier density N, electron temperature T_e, and lattice temperature T_l, subject to appropriate boundary conditions. We consider one-dimensional case (z-direction), and at the target surface ($z = 0$), the boundary condition for carrier density N is specified by

$$\left[\frac{\partial N}{\partial z}\right]_{z=0} = J_s$$

where J_s is the surface recombination rate set as zero in this study. The total carrier energy at the surface remains unchanged since the recombination process maintains the overall carrier energy.

The governing equations and boundary conditions are solved numerically using the material properties for silicon (van Driel 1987; Landolt-Bornstein, 1982). The sample thickness is chosen as 20 μm, which is large compared with the carrier diffusion depth (a couple of μm.) Standard finite difference techniques are used to solve the above equations, with a typical time step being ten femtoseconds.

A basic result from the calculations that can be directly compared with experimental data is the laser fluence threshold for silicon melting. The threshold has been calculated for 35 ps, 532 nm laser pulses (as well as infrared pulses) incident normally onto the silicon surface.

The data in figure 2.2 show the calculated maximum lattice temperature as a function of incident laser fluence (the peak value) for 532 nm laser irradiation of silicon. The melting point for silicon is approximately 1600 K, so from figure 2.2,

the threshold fluence for melting silicon is approximately 200 mJ/cm^2. This value is in agreement with experimental data (Lompre ,1984).

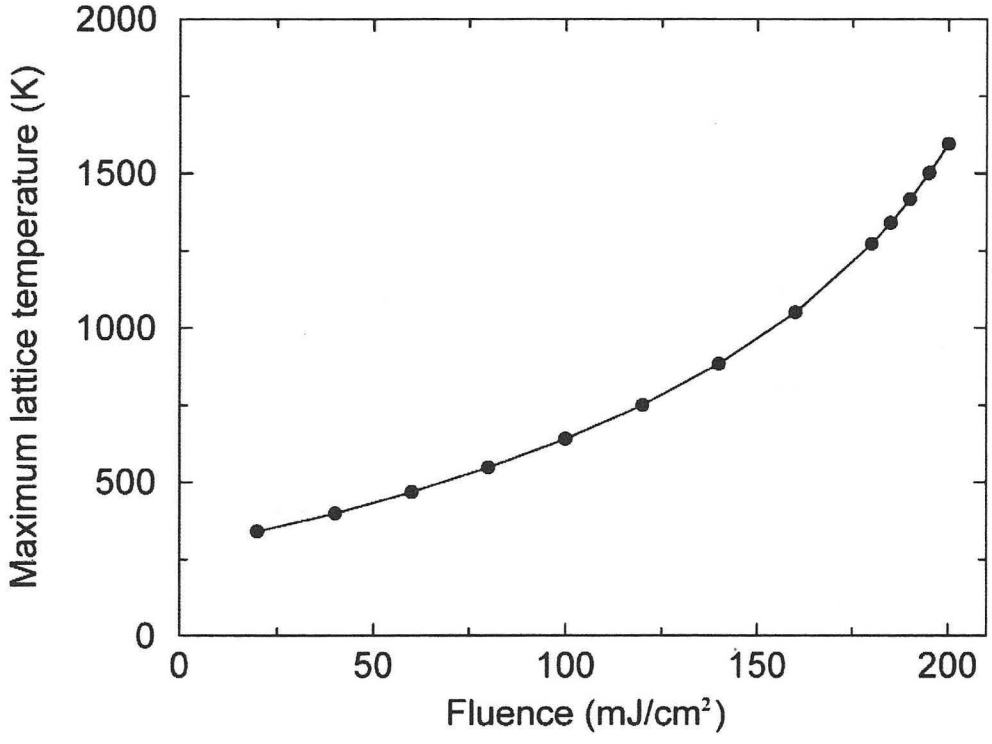

Figure 2.2. The maximum lattice temperature as a function of incident laser fluence. The melting temperature of silicon is about 1600 K.

The pulse width dependence of the fluence melting thresholds has also been calculated for incident infrared pulses (1064 nm). The simulation results are given in figure 2.3. The calculated values are in good agreement with the experimental data (Boyd et al., 1984). The agreement implies that when the incident laser pulse fluences lies below or at the melting threshold, the present model may provide quantitative information for the bulk transport processes.

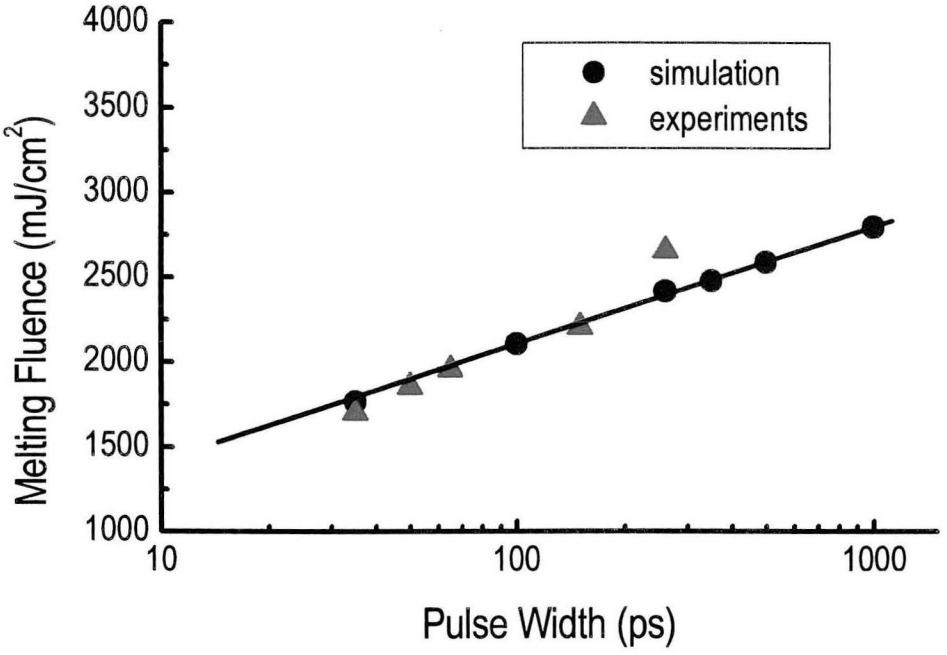

Figure 2.3. Pulse width dependence of fluence melting threshold for 1064 nm laser pulses. The experimental data are from Boyd et al., 1984.

2.4 Surface electron emission resulting from laser-material interactions

Electron emission from solid surfaces under pulsed laser excitation involves two basic mechanisms, namely surface photoemission and thermionic emission. Photoemission takes place when surface electrons absorb the energy of one or more photons to overcome the surface energy barrier and escape from the target. Alternatively, thermionic emission takes place when surface electrons possess sufficient kinetic energy to overcome the surface energy barrier.

An effective probe for studying ultrafast processes is to measure the emission of electrons from the laser irradiated target surface (Ready, 1971; Bokor, 1989). In addition, quantitative experiments and theories on electron emission resulting from thermionic and photoelectric effects at low laser pulse fluences serve as the first step in elucidating the formation mechanism of the energetic (illuminating) plasmas frequently observed at high incident fluences (Russo, 1995; and Mao et el., 1993).

2.4.1 Picosecond laser induced electron emission

Experimental investigations of pulsed laser induced electron emission from metal, semiconductor, and insulator surfaces have been reported by several researchers (Strupp, 1990; Bensoussan and Moison, 1981; Siekhaus, 1986). Theoretical studies of picosecond laser induced electron emission have been limited to the emission from metal surfaces (Anisimov et al., 1974). In the present study, we provide a theory of picosecond laser induced electron emission from semiconductor surfaces.

Silicon is chosen as a model material, since its optical and thermal properties are well characterized. Silicon is also the material on which measurements of the overall electron yields have been performed over a range of incident laser fluences (Bensoussan and Moison, 1981). Rather than employ a multi-parameter fit of the model results to experimental data, material parameters derived directly from experiments are used in the calculations. The ultimate goal of

this model is to quantify the thermionic and photoelectric emission currents and the overall electron yields when the pulse temporal profile and appropriate material parameters are specified.

Similar to the previous study of picosecond laser-semiconductor interactions, a 35 ps, 532 nm laser is used as the incident pulse source. The photon energy $h\nu$ of the laser is 2.34 eV. Since the work function ϕ of silicon is about 4.6 eV (Bensoussan and Moison, 1981), two-photon photoemission is expected to be the dominant photoelectric effect, and the expression for the photoemission current J_2 can be written as (Bechtel et al., 1977),

$$J_2 = \alpha_2 A \left(\frac{e}{h\upsilon}\right)^2 (1-R)^2 I_0^2 T_{es}^2 \Im\left(\frac{2h\upsilon - \phi}{k_B T_{es}}\right)$$

where the influence of the surface electron temperature T_{es} has been incorporated into the traditional expression for two-photon photoemission current, $J_2 \sim I_0^2$. In the above equation, I_0 is the laser pulse intensity at the target surface, R is surface reflectivity, e is electron charge, k_B is Boltzmann constant, and A is a universal constant equal to 120 A/cm^{2}K^2 (Herring and Nichols, 1949). The function $\boldsymbol{F}$ is the so-called Fowler function, its expression can be found in Bechtel et al. (1977). The coefficient α_2 is related to the electron escape probability, $\alpha_2 = 10^{-26}$ cm^{2}s/C for silicon, as derived from experiments (Bensoussan, 1981). Since the photon energy of the laser pulse is larger than the bandgap E_g of silicon (E_g = 1.12 eV at 300 K), the dominant electron emission mechanisms discussed here are expected to be different from those for wide bandgap materials (Dickinson, 1994).

Similar to photoemission, the thermionic electron emission current J_e can be described by the Richardson equation (Herring and Nichols, 1949),

$$J_e = AT_{es}^2 \exp\left(\frac{-\phi}{k_B T_{es}}\right) .$$

For all calculations of picosecond (532 nm) laser induced electron emission, the time $t = 0$ is set at the peak of the incident pulse, which has a Gaussian temporal profile with FWHM width 35 ps (Grigoropoulos, 1998). The total number of electrons produced due to thermionic emission as a function of laser fluence is shown in figure 2.4. Two distinct regimes are observed. At low incident laser intensity, the thermionic electron yields increase slowly with increasing laser fluence. For fluences above 130 mJ/cm^2, the thermionic electron yields increase very rapidly with increasing laser fluence.

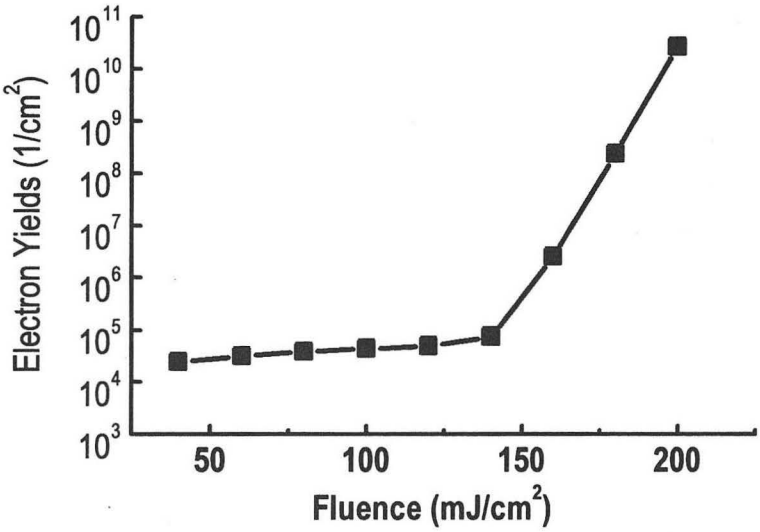

Figure 2.4. Electron yields due to thermionic emission as a function of incident laser fluence.

The two distinct regimes can be explained by considering the evolution of the electron emission current J_e and the surface electron temperature T_{es} at different fluences (figure 2.5).

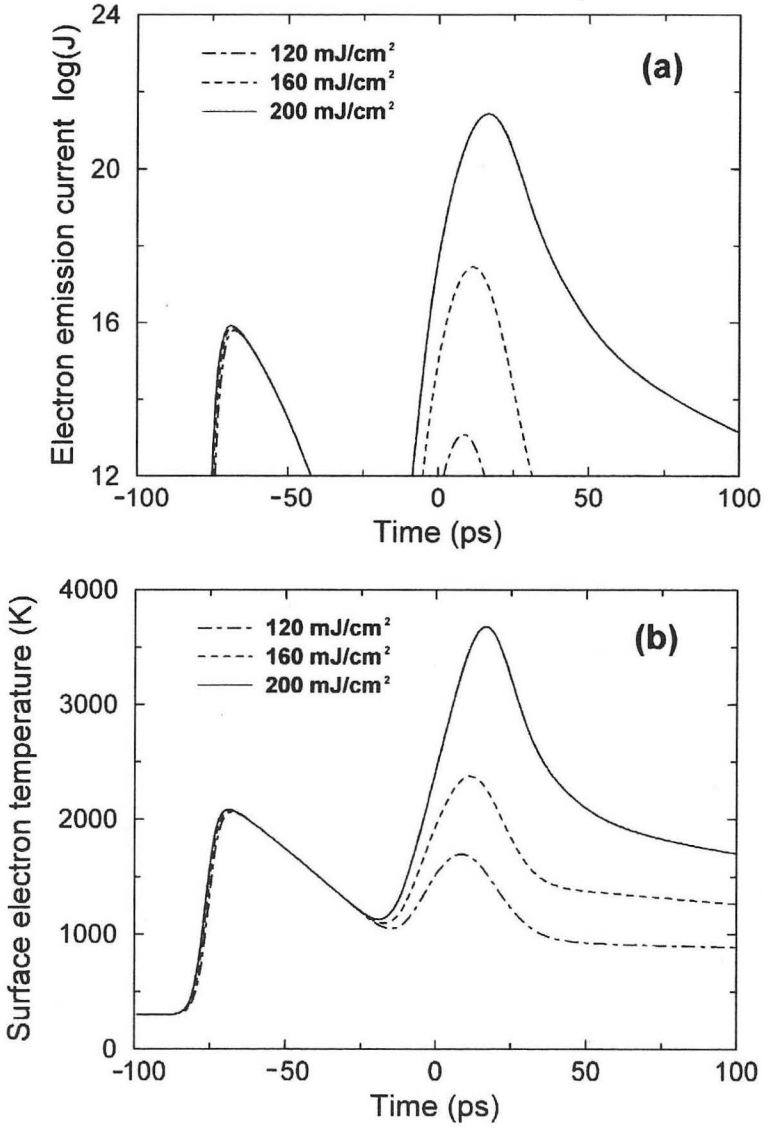

Figure 2.5. Evolution of thermionic surface emission current J_e (a) and surface electron temperature T_{es} (b) for three different incident laser fluences. The unit for J_e is $cm^{-2}s^{-1}$.

The electron emission current and surface electron temperature exhibit double-peak temporal variations (figure 2.5a), caused by the different time scales for carrier heating due to direct absorption and to Auger recombination. At the beginning of the laser pulse when the carrier density is not significantly increased, the increase in T_{es} and J_e is due to interband absorption of the pulse energy. However, near the peak of the incident laser pulse, T_{es} and J_e increase significantly because the induced high density of electron-hole pairs initiates a rapid Auger recombination process (N^3 dependence) which transfers a large amount of kinetic energy to the carriers (van Driel, 1987).

The two-regime feature can be described from the results in figure 2.5b. For laser fluences lower than about 130 mJ/cm^2, the second increase in electron temperature due to Auger recombination is smaller than the initial increase which results from interband absorption. The total number of electrons produced for low fluences depends primarily on interband absorption at the early stage of the laser pulse. The increase of J_e during the early state of the pulse is only a weak function of laser fluence (figure 2.5a).

As the laser fluence is increased above approximately 130 mJ/cm^2, the second peaks of T_{es} and J_e become greater than the first peaks, and they increase rapidly with further increases in fluence (figure 2.5). Therefore, for higher fluences, the number of electrons produced due to thermionic emission increases significantly with increasing laser fluence, indicating that the dominant mechanism

for thermionic electron emission at high fluence is due to carrier heating by Auger recombination.

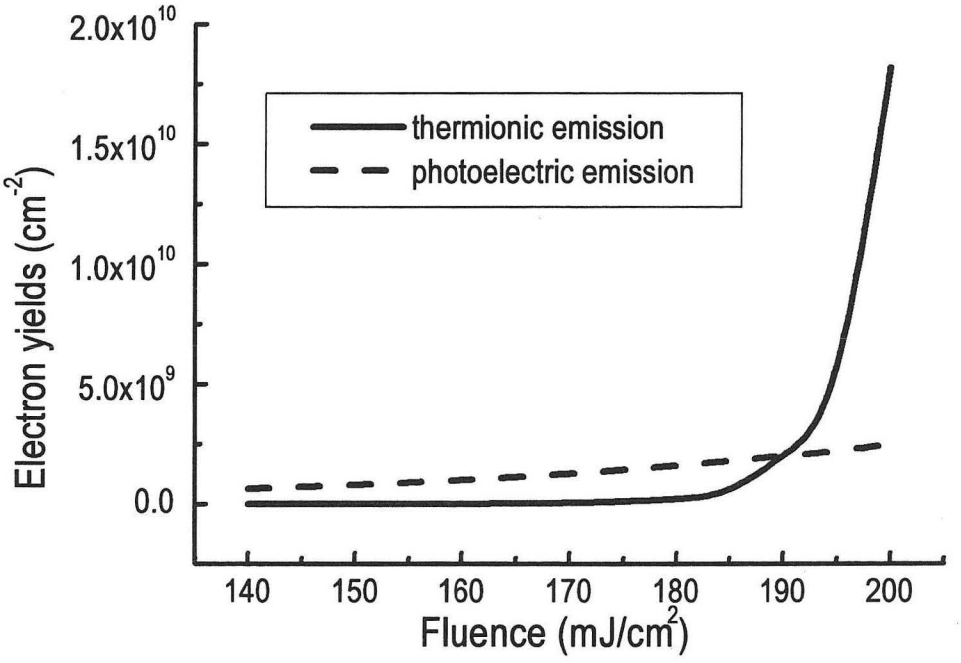

Figure 2.6. Electron yields due to thermionic and photoelectric emission as a function of incident laser fluence.

Experimentally, electrons emitted from a surface under pulsed laser excitation will include the contribution due to the surface photoelectric effect. The photoemission yields and the thermionic yields for a 35 ps, 532 nm pulses are given in figure 2.6, from which we see that for laser fluences below about 185 mJ/cm^2, the photoemission signal is larger than the thermionic emission. However, for fluences close to the melting threshold (200 mJ/cm^2,) photoemission is negligible compared to thermionic emission. This behavior may not hold for all conditions,

for example, for a picosecond infrared (1064 nm) pulse, preliminary calculations indicate that photoemission yields exceed thermionic yields for all fluences below and at the silicon melting threshold.

2.4.2 Nanosecond laser induced electron emission

For nanosecond incident pulses, previous theories usually adopted the equilibrium approximation, i.e., assuming carriers and lattice are in thermal equilibrium based on the consideration that the typical carrier thermalization times are much shorter than the laser pulse duration (Gallant and van Driel, 1982). In this study, we attempt to examine the validity of such equilibrium approximation for nanosecond laser-induced electron emission from silicon. Our approach is to solve coupled transport equations for the carriers and the lattice in semiconductor, as described in the previous sections, and determine the electron yields that can be compared with the existing experimental data.

For all calculations of nanosecond laser induced electron emission, the laser pulses are 2 ns (FWHM) Gaussian with 491 nm wavelength for varying fluences (Grigoropoulos, 1998). Calculations start 2 ns before the laser pulse reaches its peak value (figure 2.7).

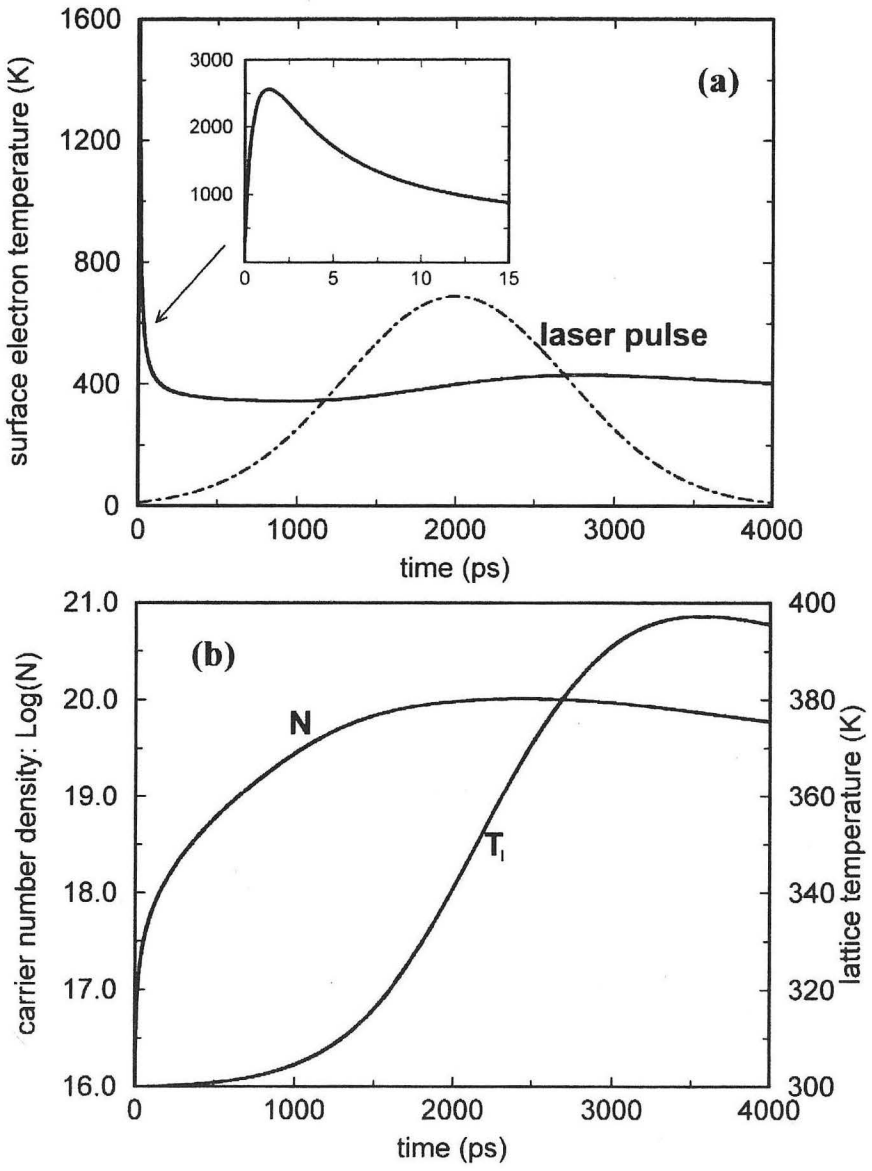

Figure 2.7. Temporal evolution of surface electron temperature T_e (a), surface lattice temperature T_l and surface carrier number density N (b), for a 2 ns laser pulse irradiation with fluence 50 mJ/cm^2. The pulse profile is also shown (arbitrary unit.) The unit for N is cm^{-3}.

The calculation in figure 2.7 show the evolution of surface electron and surface lattice temperatures, and surface carrier density, for an incident pulse fluence of 50 mJ/cm^2. At the early stage of the laser pulse (a few picoseconds), the carrier density is not significantly increased and the surface electron temperature increases significantly due to interband absorption of the incident pulse energy (figure 2.7a). After about 2 ns, a slight increase of electron temperature is also shown in figure 2.7a. At this stage, with a high density of electron-hole pairs (figure 2.7b), Auger recombination passes extra kinetic energy to the carriers and causes the carrier temperature to rise. However, such an increase is substantially smaller than the increase due to the interband absorption; therefore, at low incident laser fluences, Auger recombination is expected to have negligible effect on nanosecond laser induced electron emission.

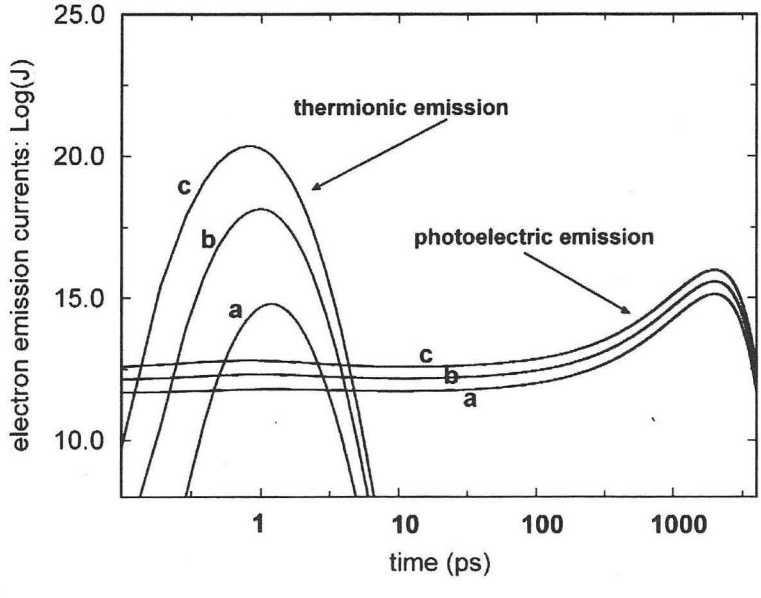

Figure 2.8. Temporal profiles of photoelectric and thermionic electron emission currents at three different laser fluences. a: 30 mJ/cm^2, b: 50 mJ/cm^2, and c: 80 mJ/cm^2.

The above conclusion is supported by the calculated temporal profiles of electron emission currents. Figure 2.8 shows the thermionic and the photoelectric electron emission currents for three different incident laser fluences. The thermionic emission currents reach a maximum at about 2 ps, but not after 2 ns, consistent with the single-photon interband absorption peak in figure 2.7a. For photoemission, the temporal evolution of the photoemission current resembles the intensity profile of the incident laser pulse (log scale in time) with a peak at 2ns.

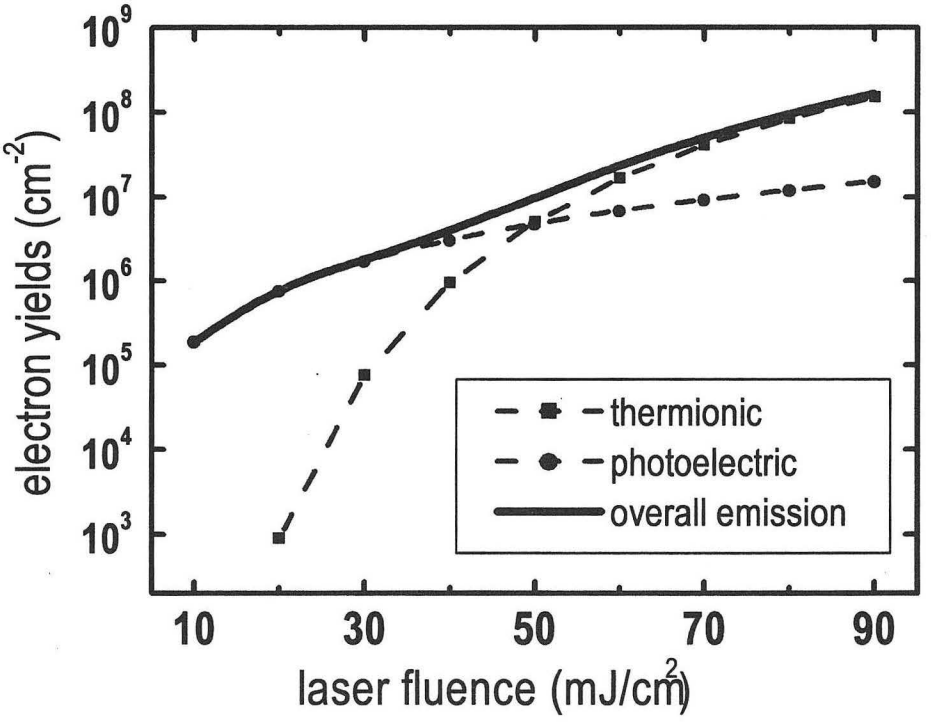

Figure 2.9. The photoelectric, thermionic, and overall electron emission yields vs. laser fluence.

The electron yields as a function of laser fluence are given in figure 2.9. At lower incident laser fluences (below 50 mJ/cm^2), electron emission due to photoelectric effect is greater than that due to thermionic effect, while above 50 mJ/cm^2, thermionic emission appears dominant. As seen from figure 2.8, thermionic emission originates from interband absorption, not from Auger recombination. This mechanism is different from the picosecond laser induced thermionic emission with incident laser fluences close to the threshold for silicon melting, where Auger recombination may be dominant (Section 2.4.1).

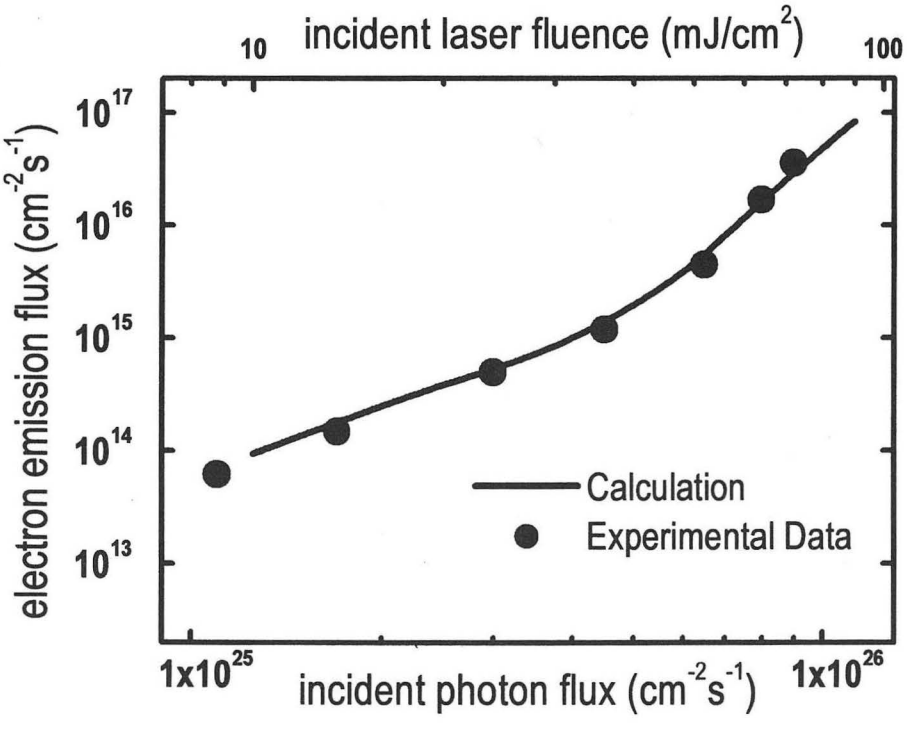

Figure 2.10. The overall electron emission flux vs. incident photon flux for 2 ns laser pulses at wavelength 491 nm.

Figure 2.10 is a log-log plot of the calculated and experimental (Bensoussan and Moison, 1981) electron emission flux as a function of incident photon flux. Two distinct regimes are observed, with the transition from photoemission due to two-photon photoelectric effect, to thermionic emission due to single-photon interband absorption, occurring at about 5 x 10^{25} $cm^{-2}s^{-1}$. This value is consistent with the experimental observation and a good agreement between the experiments and our calculations of the electron emission flux is achieved (figure 2.10.) If we had adopted the conventional equilibrium approximation that nanosecond laser-material interaction was a result of surface lattice heating ($T_e = T_l$), the maximum equilibrium temperature at the silicon surface would be below 400 K (figure 2.7b). With this approximation, the contribution resulting from thermionic emission would be negligible, and on log-log flux plot (figure 2.10), a quadratic power law characterizing two-photon photoemission would apply for all incident photon flux. However, this is not supported by the experiments.

2.5 Summary

In summary, we have studied picosecond laser-interactions with metals and semiconductors. We have extended picosecond laser heating of metals to include the melting of the target material. For the laser conditions used in this study, it was found that the target surface remains at the melting temperature (coexistence of solid-liquid phases) for only about two picoseconds. The heating of semiconductors by picosecond laser pulses was investigated based on carrier transport inside the

semiconductor material. The calculated laser threshold for silicon melting and the laser pulse width dependence were in good agreement with the existing experimental data.

An analysis was also made of surface electron emission during picosecond (35 ps, 532 nm) and nanosecond (2 ns, 491 nm) laser excitation of semiconductor silicon with laser fluences below the surface melting threshold. For picosecond laser irradiation, the calculated fluence dependence of thermionic emission yields shows two distinct regimes, which characterize a change in the dominant mechanism for carrier heating from the interband absorption of pulse energy to the Auger recombination of hot carriers. The underlying mechanism due to Auger recombination is absent in laser metal interactions.

For nanosecond laser induced electron emission from semiconductor surfaces, we have demonstrated that nonequilibrium carrier dynamics plays a significant role. While both the interband absorption of incident pulse energy and the Auger recombination processes contribute to carrier heating, for nanosecond laser irradiation with fluences well below the melting threshold, electron emission due to Auger recombination is negligible. It is found that the photoelectric effect dominates electron emission only for low incident fluences, whereas thermionic emission resulting from interband absorption is responsible for electron emission at higher incident fluences. The model results presented in this work give a satisfactory interpretation of the experimental observation of the two distinct regimes existing for nanosecond laser induced electron emission from silicon.

A direct extension of the present model would be to account for various carrier/phonon scattering mechanisms inside semiconductors. By such consideration, the relaxation-time approximation would be removed and the electrons and holes would no longer have the same temperature. In addition, instead of using the simplified phenomenological parameter - zero surface recombination rate, a set of surface rate equations would be employed as the boundary conditions coupled with bulk balance equations for electrons and holes. Such an improved model should be applicable to a wider range of time scales for laser semiconductor interactions, for example, the sub-picosecond laser induced electron emission regime where the relaxation-time approximation breaks down.

Chapter 3

PLASMA DEVELOPMENT DURING PICOSECOND LASER-MATERIAL INTERACTIONS -- EXPERIMENTS

3.1 Introduction

The formation and subsequent evolution of plasmas produced during high power laser beam interactions with solid materials (laser ablation) are topics of much practical interest. Applications include novel material synthesis (Lowndes et al., 1996; Geohegan et al., 1998), laser ablation chemical analysis (Russo, 1995), ultrafast x-ray generation (Murnane et al., 1991), and fast ignition schemes for inertial confinement fusion (Tabak et al., 1994), among others. In contrast to plasma initiation by direct photo-ionization of a free gas (Li et al., 1992; Clark and Milchberg, 1997), a plasma may be generated during laser ablation of a solid target at the focus of the incident laser beam. While substantial progress has been achieved over the past decades in understanding nanosecond laser ablation of solid materials (Wood et al., 1997; Ho et al., 1995; von Allmen and Blatter, 1995), there is little knowledge on the spatial and temporal development of plasmas induced by laser ablation of solids at picosecond time scales.

Previous investigations (Ready, 1971; Miller and Haglund, 1998) have demonstrated that laser ablation of a solid consists of several interacting stages. The initial stage is electronic excitation inside the solid (Haglund, 1996), followed by the ejection of electrons resulting from photoelectric and thermionic emission (Bechtel et al., 1977). The energetic electrons in the bulk of the solid transfer

energy to the material lattice, which results in melting and vaporization followed by the formation of a plume of material vapor, when the incident laser intensity exceeds a certain threshold. The material vapor plume absorbs incident laser energy and expands away from the target (Mao and Russo, 1997); it may interact with surrounding gases to form a shock wave and subsequently ionize ambient gases. This description of gas breakdown has been substantiated by both experiments and simulations (Ho et al., 1995; Callies et al., 1995), particularly for nanosecond laser ablation of solids.

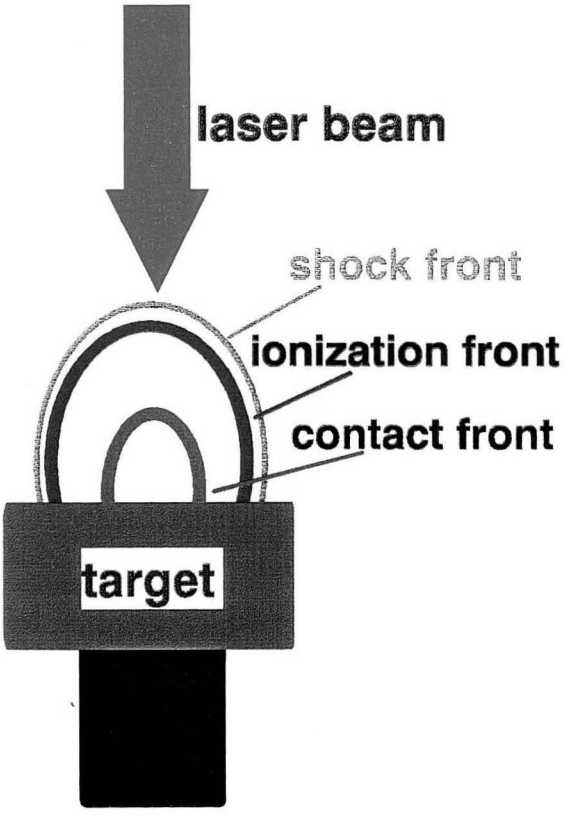

Figure 3.1. The development of plasma induced by pulsed laser ablation on nanosecond time scale.

Figure 3.1 illustrate the development of a laser ablation plasma on the nanosecond time scale. The shock wave front, the ionization front, and the contact front separating the target vapor and ambient gas are indicated in the graph. An example of nanosecond laser produced plasma from experimental observations is given in figure 3.2 (shadowgraph image).

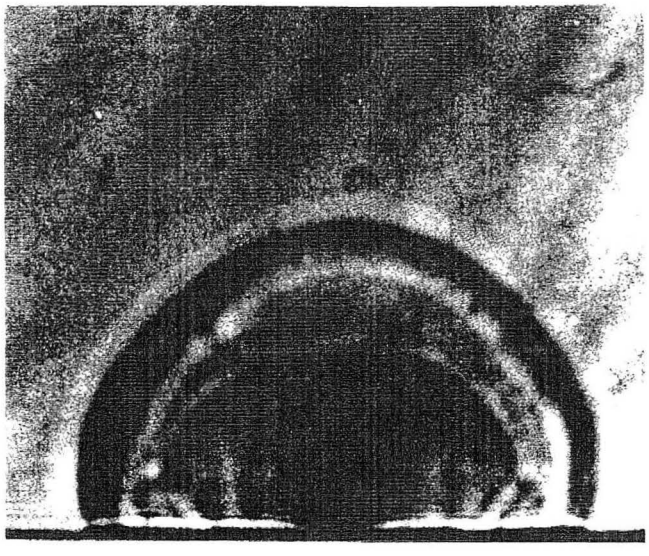

Figure 3.2. A shadowgraph image of a nanosecond laser-induced plasma above Cu target (Callies et al., 1995).

In this study, we provide experimental observations of a different type of plasma during picosecond laser ablation of copper in ambient air. Figure 3.3 shows a schematic setup of the experiments. Experiments were performed using a picosecond time-resolved Mach-Zehnder interferometer (Jahoda and Sawyer, 1971). Briefly, a Nd:YAG laser (Continuum YG601) at its fundamental wavelength (1064 nm) was used as a pump (ablation) beam with pulse duration 35 picosecond

(FWHM) and energy output on the order of 10 mJ. The laser beam was focused to a spot size of 50 to 100 μm in diameter on a pure Cu sample (polished immediately before each experiment). The second harmonic at 532 nm from the same laser was used as the probe beam; it passes an optical delay stage and forms the interferometer. By moving the delay stage, the optical path of the probe beam is varied, so the time difference between the ablation beam and the probe beam is changed. Considering that light propagates at a speed of $3x10^{10}$ cm/s, adjustment of the stage for 1 mm corresponds to a change of time difference of 6.67 ps. In the experiments, time zero (t = 0) was set when the peaks of the ablation laser beam and the probe beam overlap. When the reference path of the interferometer is blocked, a shadowgraph can be recorded by a CCD camera (Photometrics AT200) instead of an interferogram. A Fourier analysis was used to obtain a phase shift map from the interferometry measurements (Nugent, 1985). The electron number density of the plasma can be calculated from the phase shift map using an Abel inversion scheme (Deutsch and Beniaminy, 1983; Ress et al., 1994).

Using the setup in figure 3.3, an early-stage plasma with electron number density close to n_{ec} has been observed to form above the target; here n_{ec} is the critical electron density for the incident laser beam (10^{21} cm^{-3} for 1064 nm laser light). In contrast, a plume consisting of vaporized target material appears several hundred picoseconds after the laser pulse.

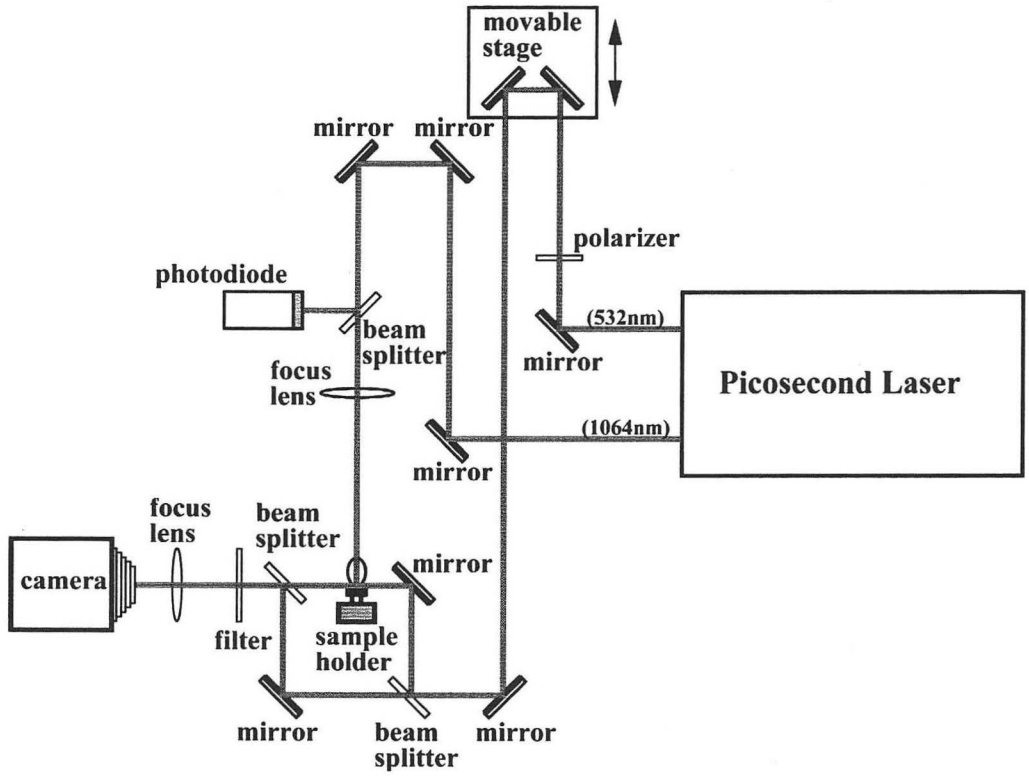

Figure 3.3. The schematic setup of the experiments. An interferometer is used to take shadowgraph and interferogram images of the picosecond laser ablation plasma.

3.2 Shadowgraph experiments

The first set of experiments we have performed was to take the shadowgraph images of the picosecond laser ablation plume. The schematic of the shadowgraph experiments is shown in figure 3.4. The probe beam (532 nm) is directed to a CCD camera after passing through a small area around the laser ablated target surface during picosecond laser irradiation. The presence of an

ablation plume will result in the absorption of the probe laser beam, a shadowgraph is therefore recorded by the camera.

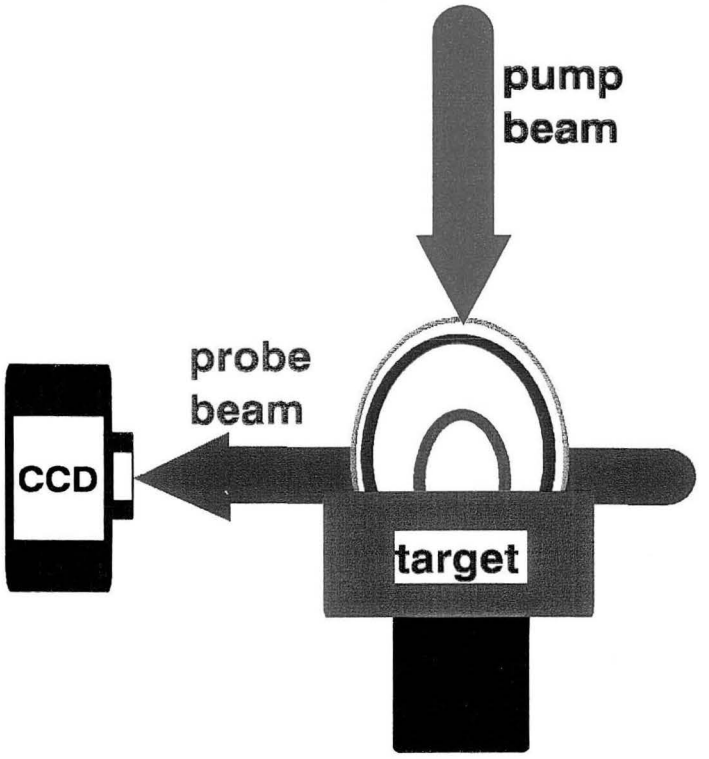

Figure 3.4. A schematic of picosecond time-resolved shadowgraph experiments.

Figure 3.5 is an example of the shadowgraph image recorded by the CCD camera when the ablation laser beam is blocked (no ablation). The target surface can be clearly seen in this figure. The fringes close to the target surface are due to edge diffraction of the probe laser beam.

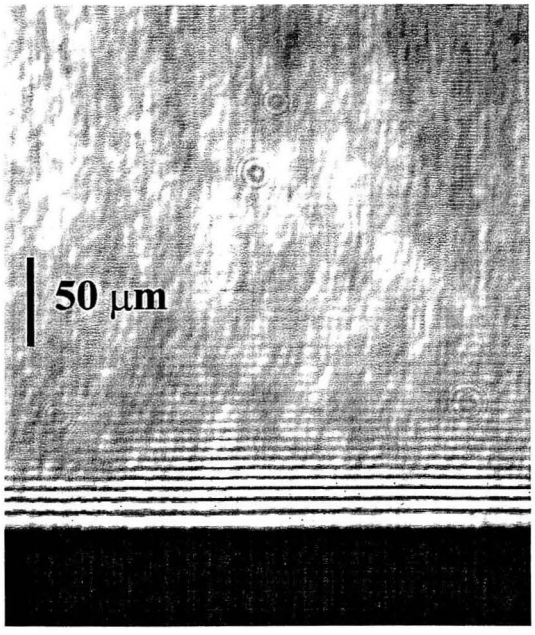

Figure 3.5. An example of shadowgraph image without laser ablation.

Figure 3.6 is a typical shadowgraph image when the laser fluence is high (10^{12} - 10^{13} W/cm^2). We find a plume adjacent to the target surface, which has a cone shape at early times (50 ps in figure 3.6). The plume has a longitudinal extent (normal to the target surface) of about 300 μm. It is a surprise to see such a plume above the laser-ablated target, because, it has been well-established that at the nanosecond time scale, the plume consisting of vaporized target material moves at a velocity of approximately 10^6 to 10^7 cm/s. This velocity value implies that the plume would advance approximately 1 to 10 μm away from the target during the picosecond laser pulse used in our experiments (35 ps pulse duration). However, what we have found is a 300 μm plume, which does not appear to possess a

hemispherical shape that nanosecond plumes have (figure 3.2). This observation suggests that the picosecond plume observed here may not consist of vaporized target material.

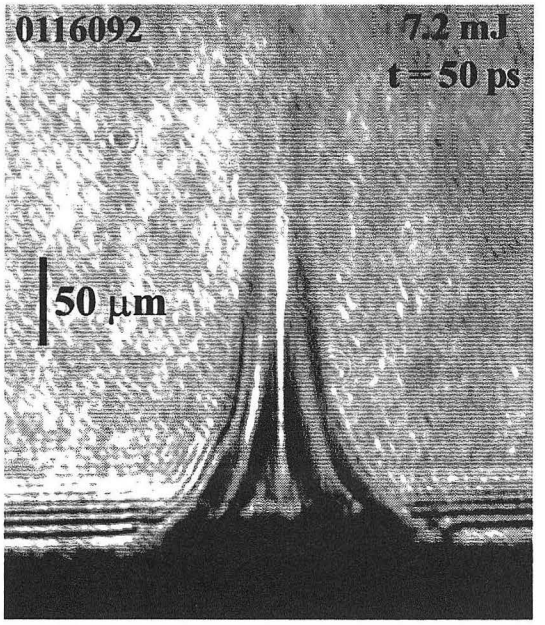

Figure 3.6. An example of shadowgraph image when a picosecond laser ablation plume is present. The experimental parameters are given in the picture.

Before we attempted to identify the cause of the picosecond laser ablation plume, we performed experiments to look at the plume formation by varying the incident laser fluence. Figure 3.7a shows three shadowgraphs taken at 20 ps delay time with different incident laser energies. The picosecond plume, or the early-stage plasma, barely appears at 3.5 mJ which corresponds to a laser irradiance of approximately 1.5×10^{12} W/cm^2. With increased incident laser energy, both the longitudinal and lateral extension of the picosecond plume increase. However, there

is no other plume present at this early time. At a delay time of 1200 ps (figure 3.7b), a hemispherical plume dominates the shadowgraph for laser energies close to the picosecond plume or plasma-forming threshold (~ 3.5 mJ). This vapor plume of target mass is frequently observed during nanosecond and longer pulsed laser ablation of solids.

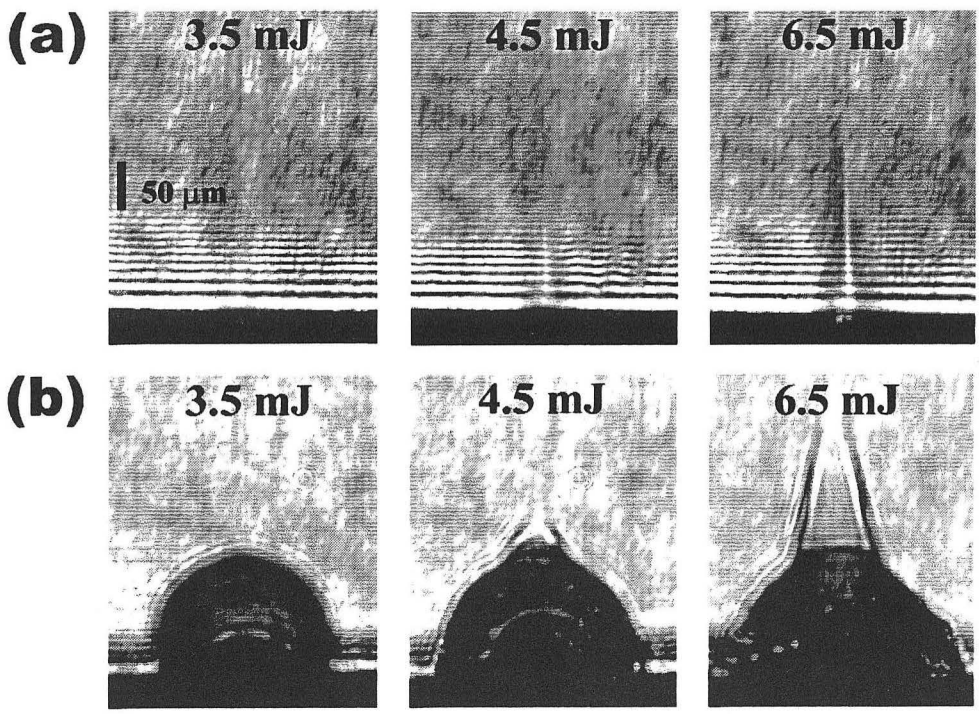

Figure 3.7. Three shadowgraph images of the laser ablation plasma at 20 ps (a) and at 1200 ps (b). The incident laser energy was given in each picture. Laser input (35 ps, 1064 nm) was from the above.

At later times (typically after 500 ps), the picosecond plume can be seen ahead of the vapor plume when the plasma-forming threshold is significantly exceeded. For 4.5 mJ or other laser energies close to the threshold, most of the picosecond plume is covered by the material vapor plume from the target. For 6.5 mJ incident laser energy (much above the threshold), a large lateral expansion of the picosecond plume is apparent; the two corresponding images at delay times 20 and 1200 ps are shown in figure 3.6. In contrast, the longitudinal expansion of the picosecond plume appears to be not very substantial over this time period.

We have performed additional experimental observations of the picosecond plume for different experimental conditions. The early-stage plasma plume was not observed using the same laser parameters if the air pressure was reduced to about one half of an atmosphere, or if the solid target was removed. The threshold laser power density for the early-stage plasma or picosecond plume is an order of magnitude lower than the threshold for photo-induced breakdown of free air (1.5 x 10^{12} W/cm^2). Direct air breakdown usually creates a plasma with longitudinal extension several times the Rayleigh length (1.5 mm in our experiments). However, the picosecond plume reported here is only about a quarter of the Rayleigh length. These observations strongly imply that the origin of the picosecond plasma plume is due to laser-target-air interactions.

3.3 Interferometry experiments

In addition to shadowgraph images of the picosecond laser ablation plume, we performed picosecond time-resolved interferometry experiments of the plume. Figure 3.8 is a schematic of the two-beam interferometry system. The probe beam (532 nm) was split into two arms, the reference arm and the detection arm, both of which were mixed in front of a CCD camera (and a single pass filter for 532 nm light beam). Fixed optical path difference between the two arms generates background interference fringe patterns as seen in figure 3.9.

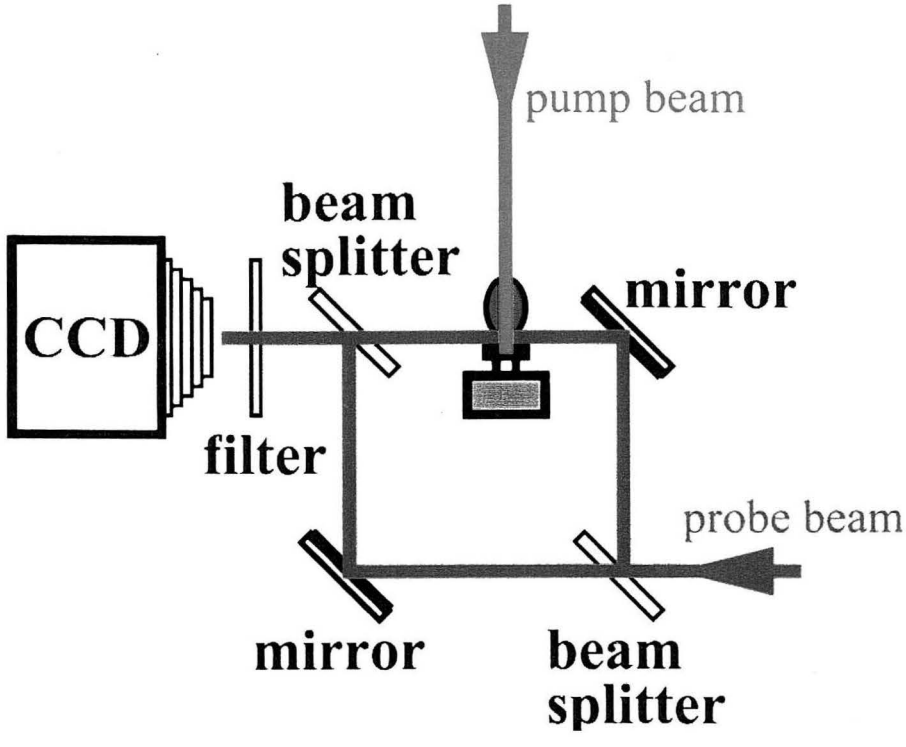

Figure 3.8. A schematic of picosecond time-resolved interferometry experiments.

Figure 3.9 is a typical time resolved interferogram of the picosecond plume. The appearance of a plasma plume above the laser ablation target will change the

optical path of the probe beam at the detection arm. Therefore, a shift of the interference fringes results close to the target surface (figure 3.9). The longitudinal (z) and lateral (r) directions have also been identified in this figure.

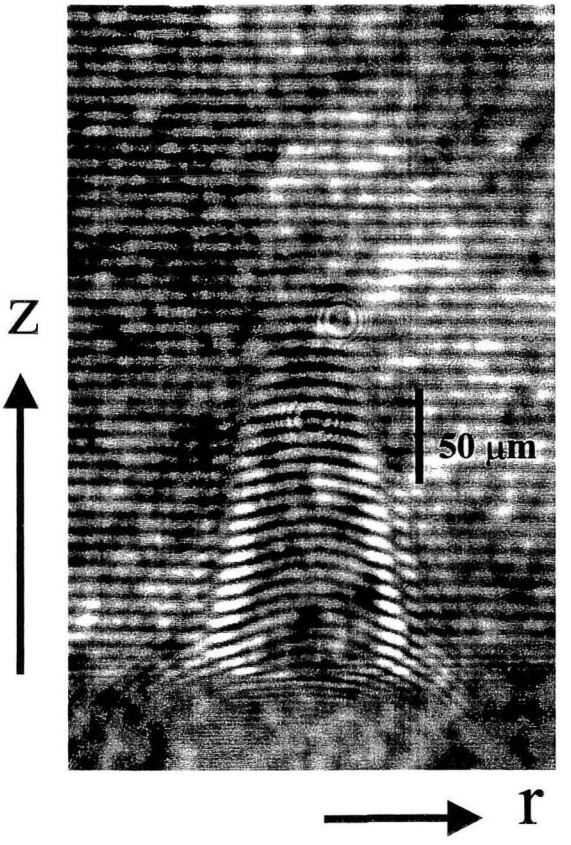

Figure 3.9. An example of the interference pattern of a picosecond laser ablation plasma. The picture was taken at 15 ps delay time.

At the very early time during the laser ablation process ($t \sim 0$), the plasma plume was found to have an electron number density on the order of 10^{19} cm^{-3} near the target surface. Figure 3.10 shows the plume's electron number density profile

along the incident laser axis at 150 ps delay time. The solid curve is a least-square fit for an exponential decay. The plasma has an electron number density exceeding 10^{20} cm^{-3} from the target surface within a distance approximately 40 μm away from the target.

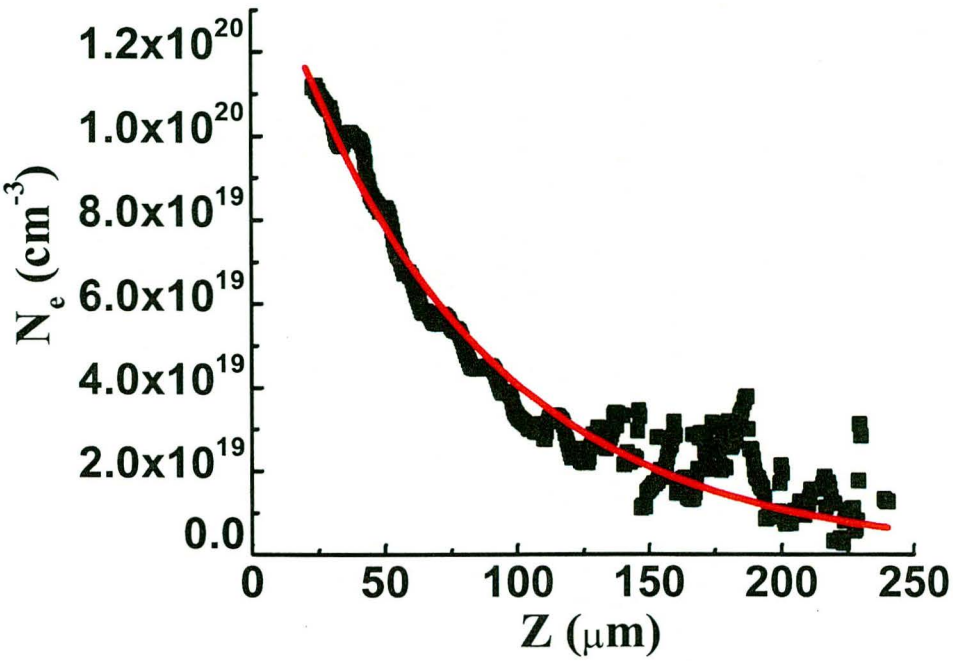

Figure 3.10. Electron number density profile along the incident laser axis. The solid curve is a least square fit of the experimental data showing exponential decay.

This large number of electrons (close to the target surface) indicates that the electrons cannot originate from direct air ionization. The ambient air has a density between 2 and 3 x 10^{19} cm^{-3}. If the electrons inside the plasma come from direct air ionization, each air molecule would have to provide about ten free electrons. This is

impossible in our case because the plasma temperature (Chapter 4) barely exceeds the second ionization potential of the atoms (e.g., nitrogen) in air. The high electron density (many times larger than air density close to the target) suggests that electrons emitted from the target surface play a significant role for the initiation of this early-stage plasma. Energetic electrons have been detected (Petite et al., 1992) from metal surfaces irradiated by picosecond laser pulses, although their importance for plasma initiation was not previously realized.

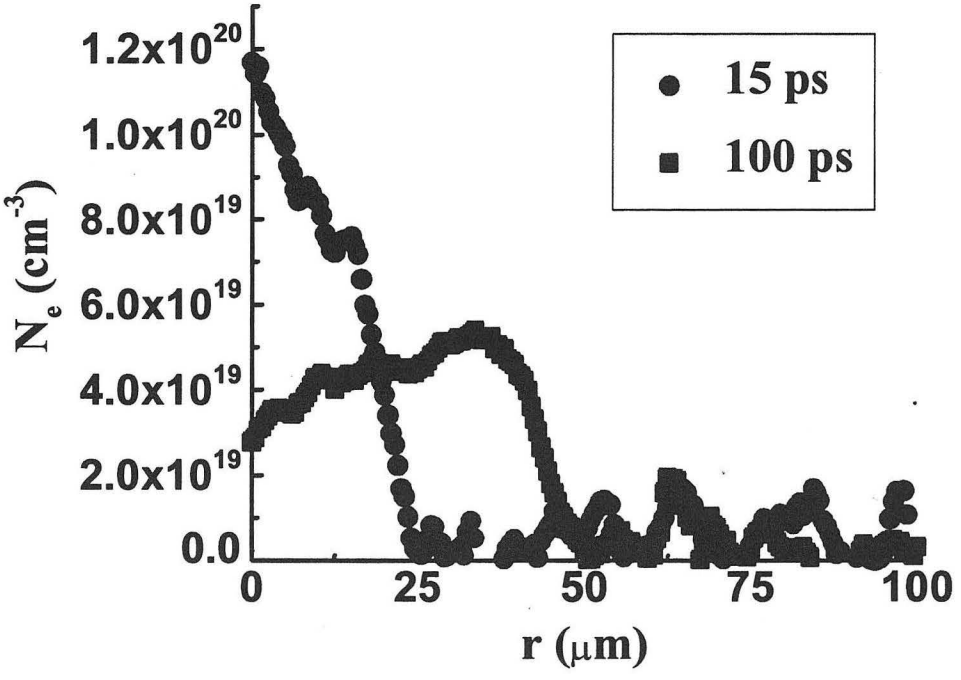

Figure 3.11. Lateral electron number density profile of the picosecond laser ablation plasma at delay time 15 ps and 100 ps respectively.

The radial electron number density profiles near the target during and after the 35 ps laser pulse are illustrated in figure 3.11. At a 15 ps delay time, the electron density profile exhibits a maximum centered along the incident laser axis. At 100 ps after the laser pulse has ended, the plasma forms an electron depletion profile with a high electron density near the radius and a low density region along the incident laser axis.

3.4 Summary

The picosecond time resolved shadowgraph and interferometry experiments reported in this chapter provide novel insights of the initial phase of plasma formation during picosecond laser ablation of solids. The general characteristic of the laser ablation plasma - an early-stage gas plasma ahead of a material vapor plume - has been observed for the first time. The experimentally measured large electron number density in this early-stage plasma suggests that they originate primarily from the target instead of from direct photo-ionization of the air. The lateral electron density profile of the plasma has also been measured, the results indicate that an electron depletion region is formed along the laser axis after the laser pulse is completed.

Chapter 4

PLASMA DEVELOPMENT DURING PICOSECOND LASER-MATERIAL INTERACTIONS -- THEORY

4.1 Introduction

As discussed in Chapter 3, we have performed picosecond time-resolved experiments on plasma formation during picosecond laser ablation of solids in air. In contrast to the explosion of a material vapor plume (Wood et al., 1997; Ho et al., 1995), which appeared several hundred picoseconds after the ablation laser pulse (35 ps FWHM), we found an early-stage plasma developing during the picosecond laser pulse. Interferometry measurements indicate that, close to the target surface, the plasma has an electron number density, n_e, on the order of 10^{20} cm^{-3}. Such a high value of n_e suggested that electrons emitted from the target surface play a significant role for the initiation of the plasma.

In this chapter, we report on the development of a one-dimensional model for the initiation and evolution of the picosecond laser ablation plasma. The simulation results are successful in describing the experimental observations.

4.2 A Laser-solid-plasma interaction model

Copper was selected as the target material in our model because a large set of experimental data on the plasma are available. For comparison with existing measurements, the ablation laser pulse simulated (1064 nm) was a Gaussian beam with 35 ps pulse duration (FWHM). The peak fluence of the laser pulse was 150

J/cm^2. Initially, the ambient gas (nitrogen) remains static at room temperature (300 K) and atmospheric pressure. The semi-infinite Cu target, with its surface chosen as $z = 0$, was also at 300 K. Time zero ($t = 0$) was set at the peak of the ablation laser pulse.

The model we have developed consists of two parts. The first one is picosecond laser heating of the target material, and the second one is plasma development above the target. At the early rising stage of the picosecond laser pulse ($t < 0$), absorption of laser radiation by the Cu target leads to elevated surface electron and lattice temperatures (Anisimov et al., 1974; Qiu and Tien, 1993). As discussed in Chapter 2, electrons inside the Cu target absorb laser energy and become energetic. Through electron-lattice collisions, the electrons pass energy to the lattice therefore raising the material temperature. A schematic of the picosecond laser heating process is illustrated in figure 4.1.

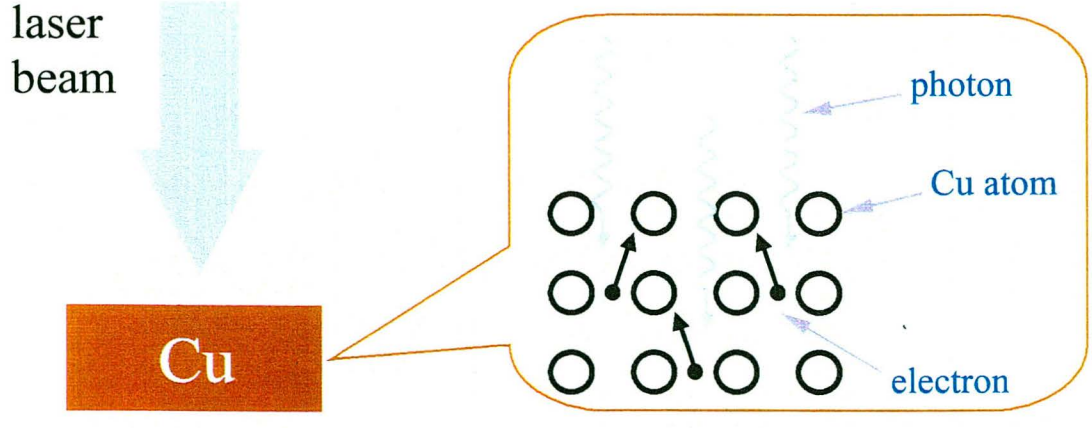

Figure 4.1. A schematic illustration of picosecond laser heating of copper (photon-electron-phonon interactions).

The energy transport equations for picosecond laser heating of a metal have been discussed in Chapter 2. Here the balance equations for electrons and lattice energy inside the target material are provided,

$$\frac{\partial \varepsilon_e}{\partial t} = -\nabla \cdot q_e + W_L - U_{e-l}$$
$$\frac{\partial \varepsilon_l}{\partial t} = -\nabla \cdot q_l + U_{e-l}$$

with ε_e and ε_l, the electron and lattice energy, respectively.

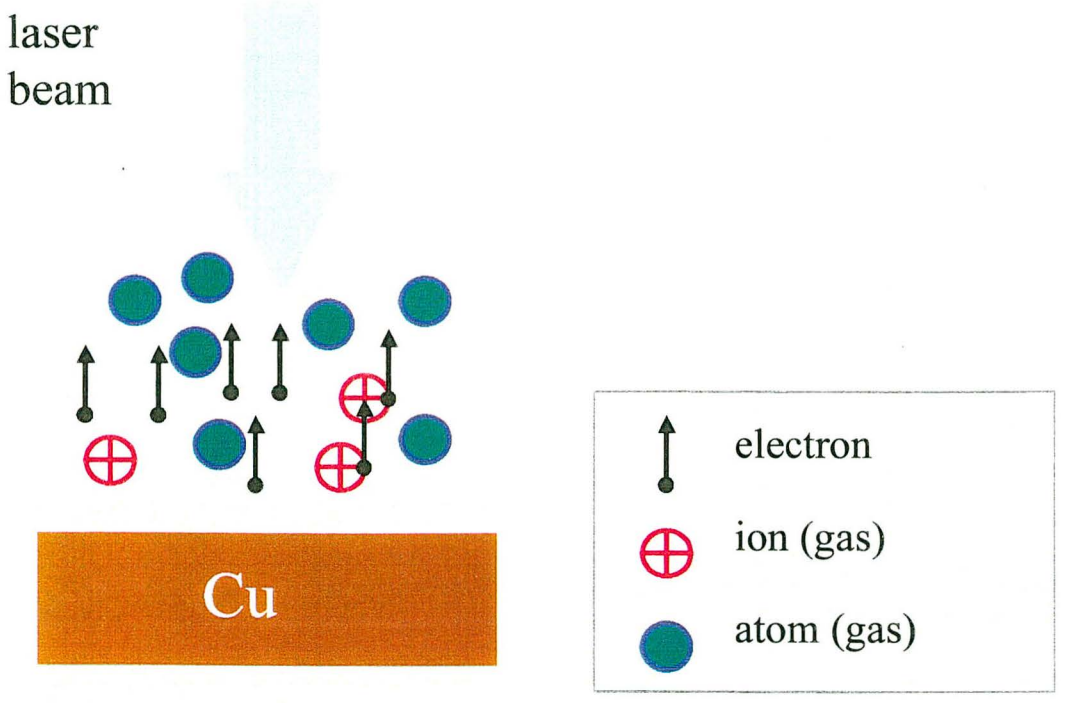

Figure 4.2. A schematic illustration of the plasma plume induced by picosecond laser ablation of copper.

Plasma development above the laser ablated target is calculated based on conservation laws for each species (electrons, ions, and atoms) present in the

plasma (figure 4.4) (Kruer, 1988). Electrons, neutral gas atoms, and ionized gas ions (positively charged) are included in our simulation (Spitzer, 1956; Hora, 1991).

The conservation of particle number density n, momentum p, and energy ε can be expressed as

$$\frac{\partial n}{\partial t} + \frac{\partial (n \cdot u)}{\partial z} = S_n$$
$$\frac{\partial p}{\partial t} + \frac{\partial (p \cdot u)}{\partial z} = -\frac{\partial P}{\partial z} + nqE + nf_c$$
$$\frac{\partial \varepsilon}{\partial t} + \frac{\partial (\varepsilon \cdot u)}{\partial z} = -\frac{\partial (P \cdot u)}{\partial z} + nqE \cdot u + nf_c \cdot u + W_L$$

with u representing the velocity of the particle species inside the plasma, P the particle pressure, q the unit charge of an electron, E the electric field inside the plasma, f_c the collisional force between particles, and W_L the energy source due to absorption of laser light.

The particle momentum and energy are given by

$$p = nmu$$
$$\varepsilon = \frac{3}{2} nk_B T + \frac{1}{2} nmu^2$$

where m is particle mass, T is particle temperature, and k_B is the Boltzmann constant.

In the density equation, S_n is the source term for electron and ion generation in the bulk of the plasma. Cascade ionization is the dominant ionization mechanism over multi-photon and recombination processes. In the momentum equation, we included the electric force (zero for atoms) and the force resulting from particle-

particle collisions. The nonlinear (ponderomotive) force (Kruer, 1988), which is important for the propagation of high intensity laser pulses in plasma (Young et al., 1988), was found to be insignificant in the laser energy range of the present study. In the energy equation, we included the work done by the forces exerted on particles, as well as the direct energy increment from absorbing laser light (for electrons only).

As discussed in Chapter 2, electron emission takes place as the surface electrons absorb the energy of one or more incident photons, or acquire sufficient kinetic energy after heating, to overcome a surface energy barrier. A unique feature of our model is the implementation of surface electron emission as one boundary condition. We allow electron emission to provide initial seed electrons for plasma development above the laser ablated target. While pulsed laser induced electron emission from solids has been studied for decades, its significance for the initiation of laser ablation plasmas has not been quantified in previous theoretical work. In our simulation, surface electron emission due to thermionic and photoelectric effects was calculated using a coupled energy transport model (for electron and lattice energies) for picosecond laser-metal interactions.

Standard finite difference techniques (LeVeque, 1992; Tannehill et al., 1997) were employed to numerically solve the coupled plasma equations discussed above. The typical time step in the calculations was a fraction of a femtosecond. Figure 4.3 illustrates a schematic process for plasma development. The electrons

emitted from the laser-heated target collide with atoms in the ambient gas, which may result in cascade breakdown of the gas.

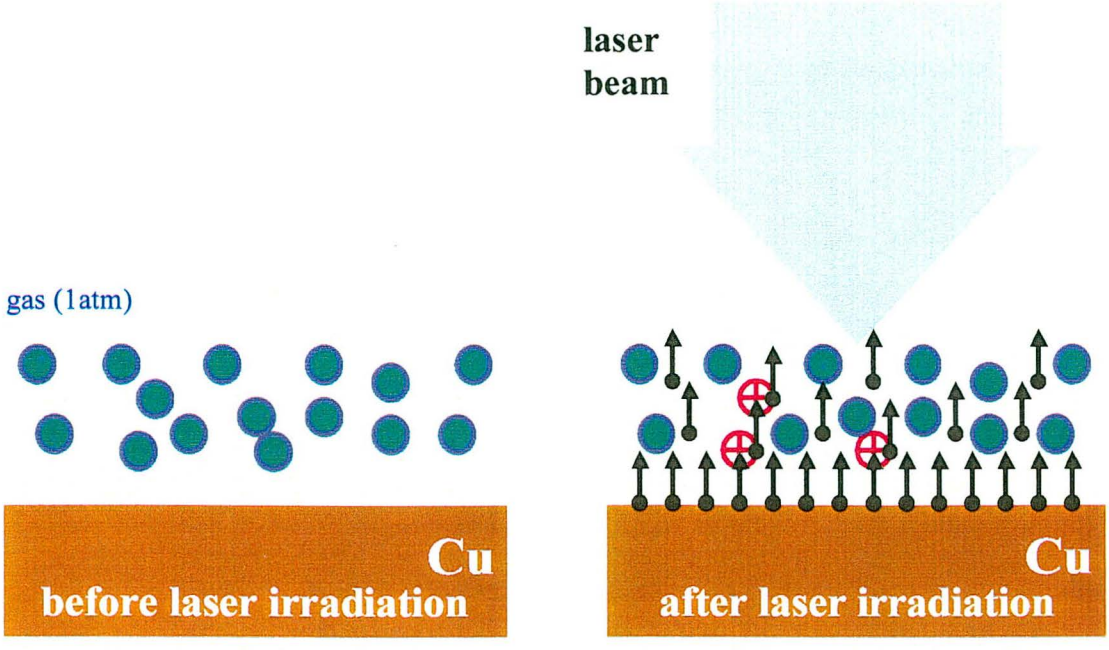

Figure 4.3. A schematic illustration of plasma development, before and after picosecond laser irradiation of copper target. Atoms and ions can be approximated at immobile because they have a much larger mass than electrons.

4.3 Theoretical results and discussions

Figure 4.4 shows the evolution of ion and atom densities above a Cu target. In the color map for ions (atoms), blue color corresponds to a high density of ions (atoms). With n_i and n_a representing the ion and atom density respectively, full-ionization of the gas, $n_i \sim n_a$ (1 atm), occurs at the time when the ablation laser pulse reaches it maximum energy. As evident in figure 4.4, significant ionization

starts in the gas adjacent to the target surface where energetic electrons abound due to surface electron emission during the rising stage of the picosecond laser pulse.

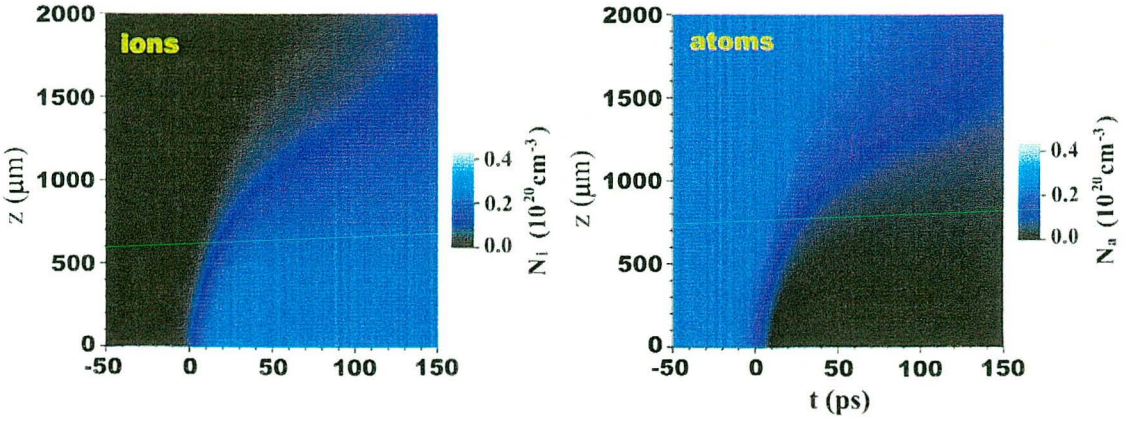

Figure 4.4. Spatial-temporal evolution of ion and atom density inside plasma. Pseudo-colors are used to represent the magnitude of the densities.

The electrons ejected from the target absorb laser energy principally by inverse Bremsstrahlung processes during laser irradiation. They subsequently impact ionize the ambient gas, leading to cascade breakdown. The spatial-temporal movement of the ionization front is characterized by an approximate boundary separating the blue and black regions in the color map for both ions and atoms. The ionization front advances approximately 750 μm during the first 35 ps (from approximately 0 ps to 35 ps), but it requires more than 100 ps to reach the next 750 μm (figure 4.4).

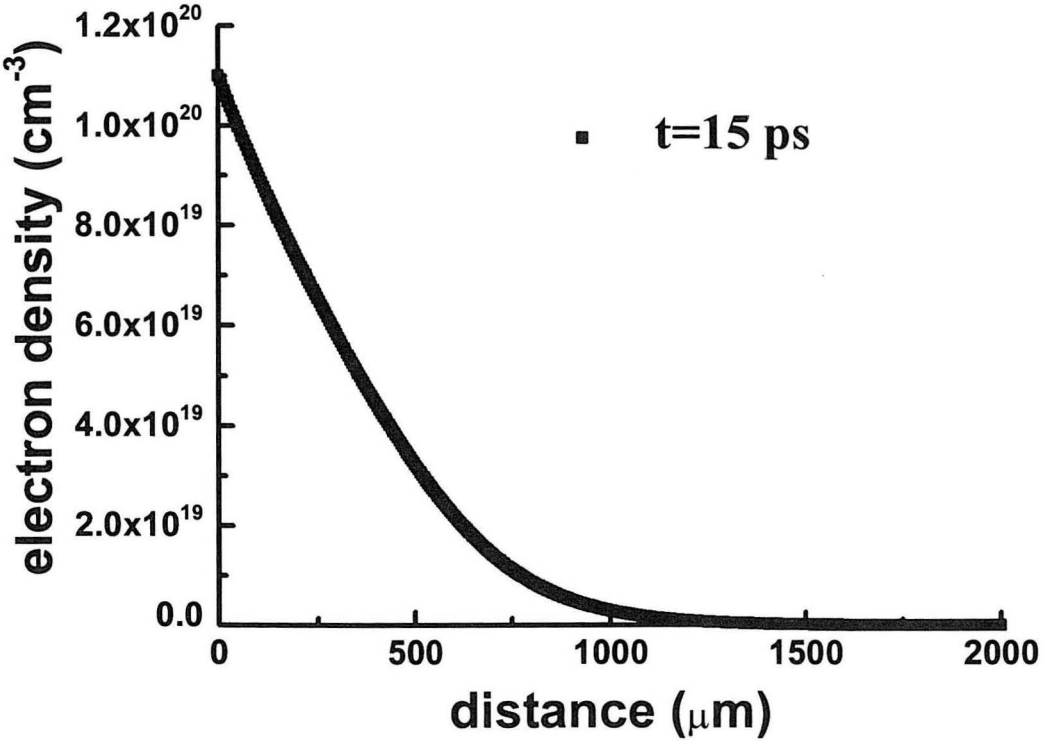

Figure 4.5. Calculated longitudinal electron number density profile of the picosecond laser ablation plasma at 15 ps delay time.

Figure 4.5 shows a calculated longitudinal electron number density profile (along the z direction) of the picosecond laser ablation plasma at 15 ps after the peak of the ablation laser pulse. In agreement with the experimental measurements, the electrons have a number density on the order of 10^{20} cm^{-3} close to the target surface. Far from the target, the calculated electron density is slightly larger than

experimental measurements. Lateral (radial) electron movement has been ignored in the one-dimensional approximation.

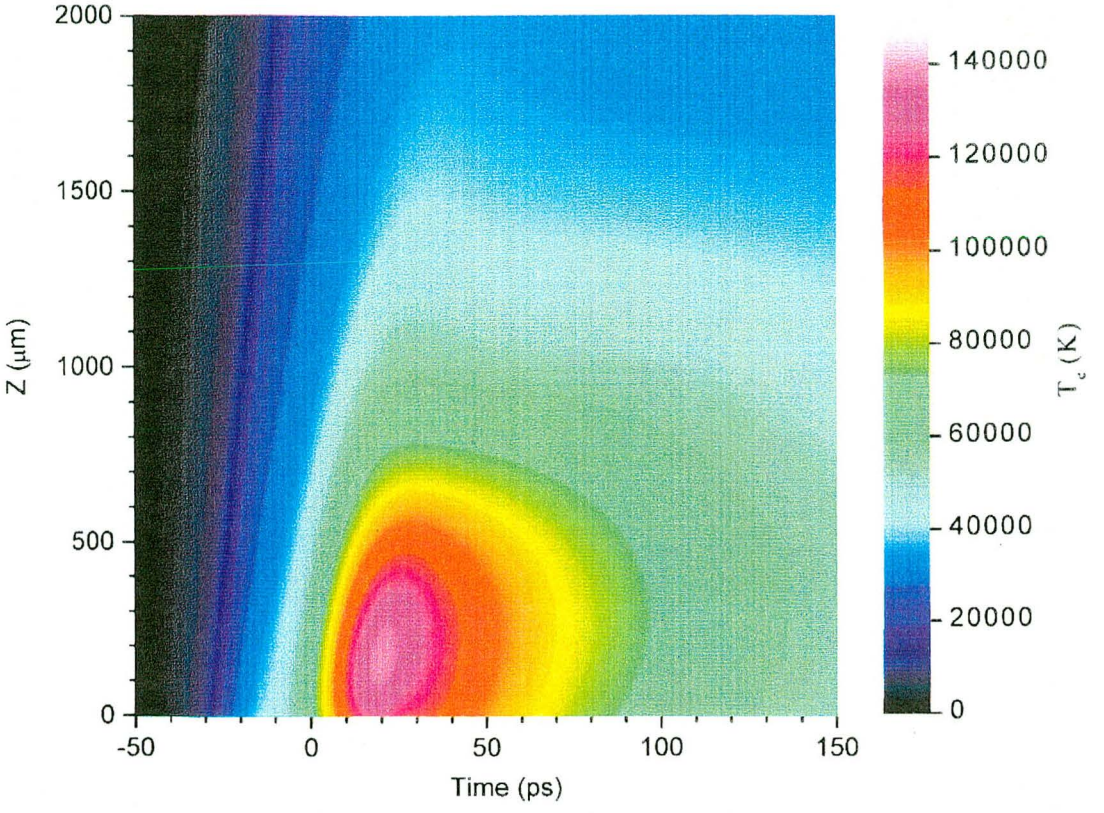

Figure 4.6. Spatial-temporal evolution of electron temperature of the picosecond laser ablation plasma.

We have also calculated the electron temperature inside the picosecond laser ablation plasma. Figure 4.6 gives the temperature profile in a spatial-temporal diagram. As evident from the picture, electrons reach their maximum temperature just after the laser intensity passes its peak value (t = 0). The temperature of the

plasma is on the order of 10^5 K, equivalent to about 10 eV. This value is approximately equal to the first ionization energy of atoms in ambient gas, but smaller than their second ionization energy. As a consequence, we expect that most of the ions in the plasma have only one positive charge. This result suggests that a gas atom can provide at most one free electron to the plasma. The experimentally measured large number of electrons cannot come from laser-induced direct gas breakdown. Electron emission from the target surface, as discussed earlier, will supply a large quantity of electrons to the plasma.

4.4 Summary

The simulation presented here provides clear evidence for plasma initiation above the laser ablated target at the picosecond time scale. In agreement with experimental observations, the picosecond laser ablation plasma started to develop from the ambient gas close to the target surface. The calculated spatial profile of the electron number density of the plasma is consistent with the measured data. Laser-induced electron emission from the target surface was found to play a significant role for plasma formation by providing seed electrons for laser-induced gas breakdown above solids. In contrast to previous simulations of laser ablation plasmas, we incorporated picosecond laser-induced electron emission as one boundary condition for plasma development. Combined with the measurements that the laser intensity threshold for plasma formation is about one order of magnitude larger than that for direct gas breakdown, we conclude that the origin of

the picosecond plasma is due to electron emission assisted breakdown of ambient gas during the picosecond laser pulse.

In addition, we found that the temperature of the electron-dominant plasma is on the order of the first ionization energy of the atoms inside the ambient gas; second ionization of the gas is not expected to be significant. Picosecond time-resolved spectral experiments would be valuable to verify this simulation result.

Chapter 5

DYNAMICS OF PICOSECOND LASER INDUCE PLASMA ABOVE SOLIDS

5.1 Introduction

We have studied the characteristics of the picosecond laser ablation plasma in Chapter 3 and 4. In this chapter, we present picosecond time-resolved measurements of plasma dynamics. We measure the expansion of the plasma in both the longitudinal and lateral directions.

The experimental setup for observing plasma dynamics has been described in chapter 3; a Mach-Zehnder interferometer is used to monitor the plasma development above the solid surface during and after laser irradiation. Important features of the longitudinal plasma expansion are reproduced from the one-dimensional model established in Chapter 4. For lateral plasma expansion, experimental data will be compared with the similarity theory for a two-dimensional blast wave.

5.2 Longitudinal expansion of picosecond laser-induced plasma

Figure 5.1 shows shadowgraphs (a) and phase shift maps (b) of the picosecond laser ablation plasma at four different delay times. The phase shift value of the interference fringe is directly proportional to the value of local electron number density (Jahoda and Sawyer, 1971). The laser energy was approximately 9 mJ for pictures in figure 5.1, which corresponds to a laser irradiance of

approximately 4 x 10^{12} W/cm^2. As discussed in Chapter 3, at time zero, a weakly absorbing plasma is present with an electron number density on the order of 10^{19} cm^{-3} near the target surface.

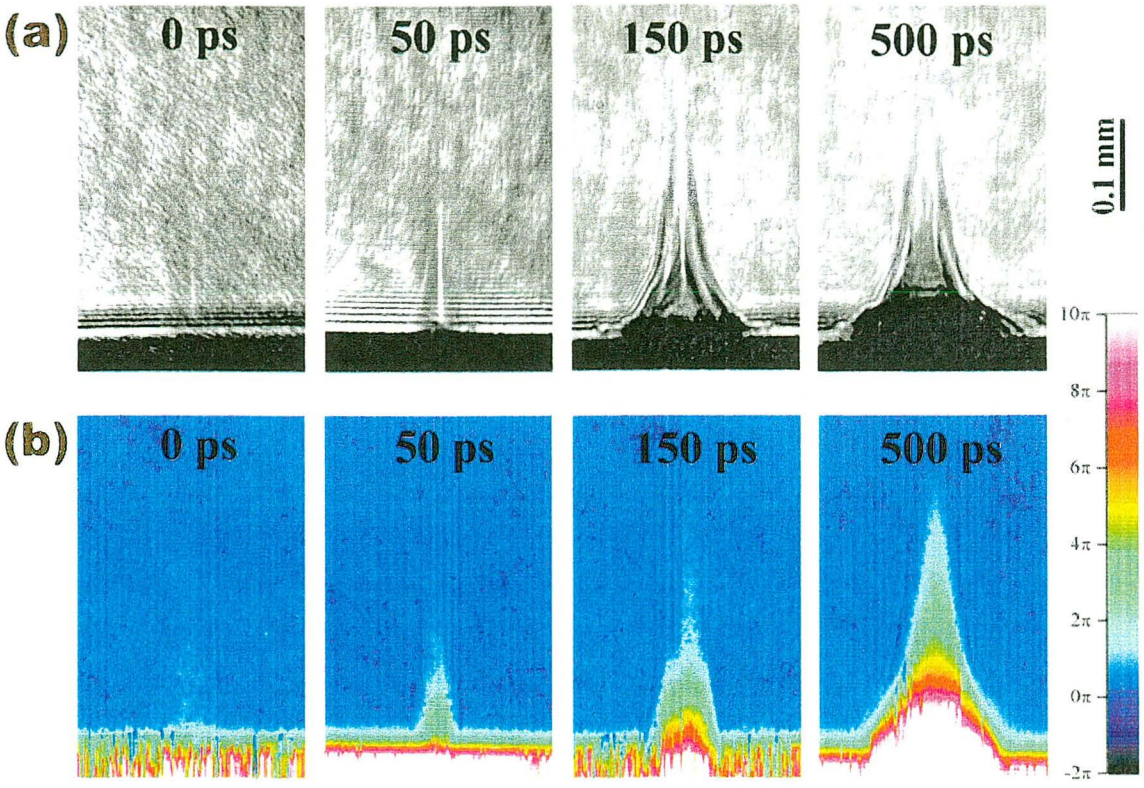

Figure 5.1. Shadowgraphs (a) and phase shift maps (b) of the picosecond laser ablation plasma at four different delay times.

The color phase shift maps (figure 5.1b) indicate that the electron number density of this plasma increases substantially during the first 100 picoseconds. After about 200 picoseconds, atomic and ionic mass from the target appear in the shadowgraphs (dark region close to the target). This material vapor plume corresponds to a growing white area in phase shift maps, where the strong

absorption of the probe beam weakens the resolution of the interferogram and no longer yields useful phase shift values. As the material vapor plume expands away from the target, it gradually becomes hemispherical in shape (figure 5.1b).

As seen in figure 5.1, large lateral expansion of the picosecond laser ablation plasma is apparent, while the longitudinal expansion of the early-stage plasma is not very substantial after about 200 ps.

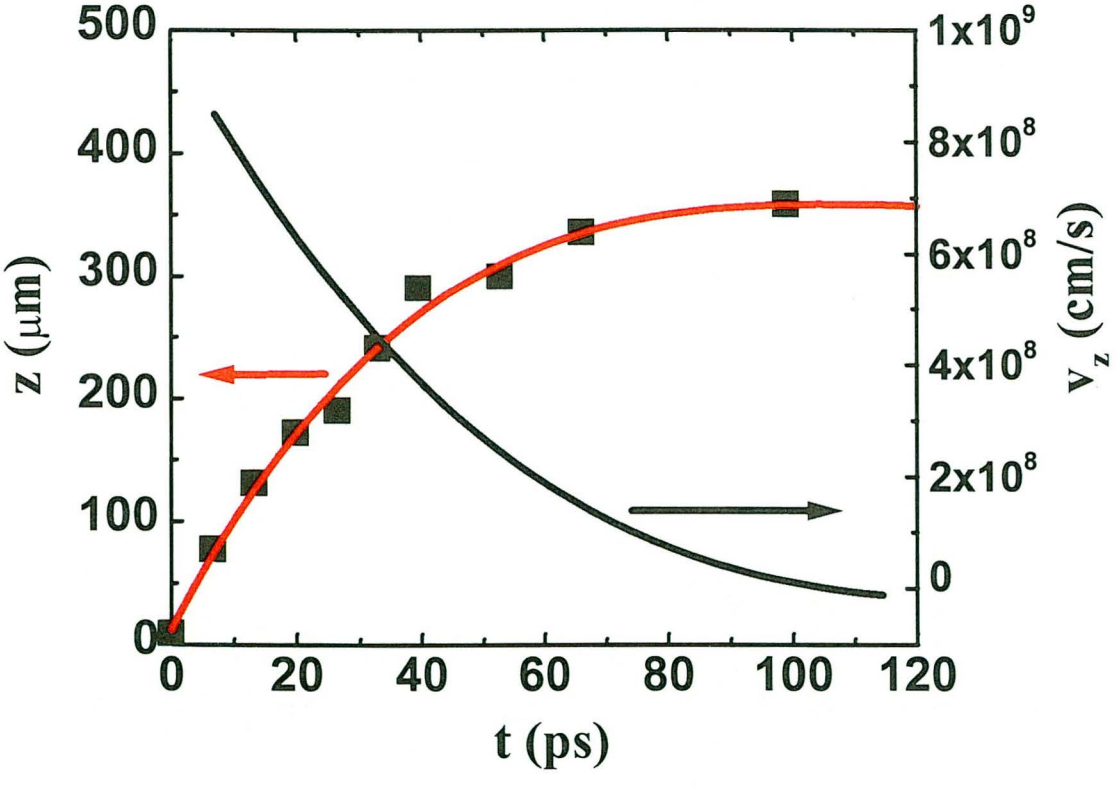

Figure 5.2. Temporal variations of the measured longitudinal distance and expansion velocity of the picosecond plasma.

Figure 5.2 shows the longitudinal extent of the picosecond plasma as a function of time. The solid curve is a polynomial least square fit to the experimental data, from which the expansion velocity was calculated. Initially, the longitudinal plasma expansion velocity exceeds 10^9 cm/s, but decreases rapidly after the laser pulse. Such a suppression of longitudinal plasma expansion is not expected and its cause is not apparent from the observations.

We have also performed a simulation of the longitudinal dynamics of the picosecond laser ablation plasma. Details of the model have been discussed in Chapter 4. Figure 5.3 shows calculated electron number density profiles in the form of iso-density contours. These distance-time profiles provide a measure for the longitudinal expansion of the plasma. As shown in figure 5.3a, the electron density near the target surface increases from 6 x 10^{19} cm^{-3} to 10^{20} cm^{-3} in about 15 picoseconds (from -5 ps to 10 ps), in agreement with the experimental observations. With speeds on the order of 10^8 to 10^9 cm/s, the iso-density fronts expand rapidly at early times. However, after approximately 35 ps when most of the laser pulse energy has been delivered, the 10^{20} cm^{-3} front starts to move backward, while the 6 and 8 x 10^{19} cm^{-3} fronts expand at significantly reduced speeds. This suppression of the longitudinal plasma expansion is consistent with the experimental measurements. The experimental results that correspond to an electron density of 7 x 10^{19} cm^{-3} are given in figure 5.3b. The insert is a series of plasma shadowgraphs taken at four different delay times.

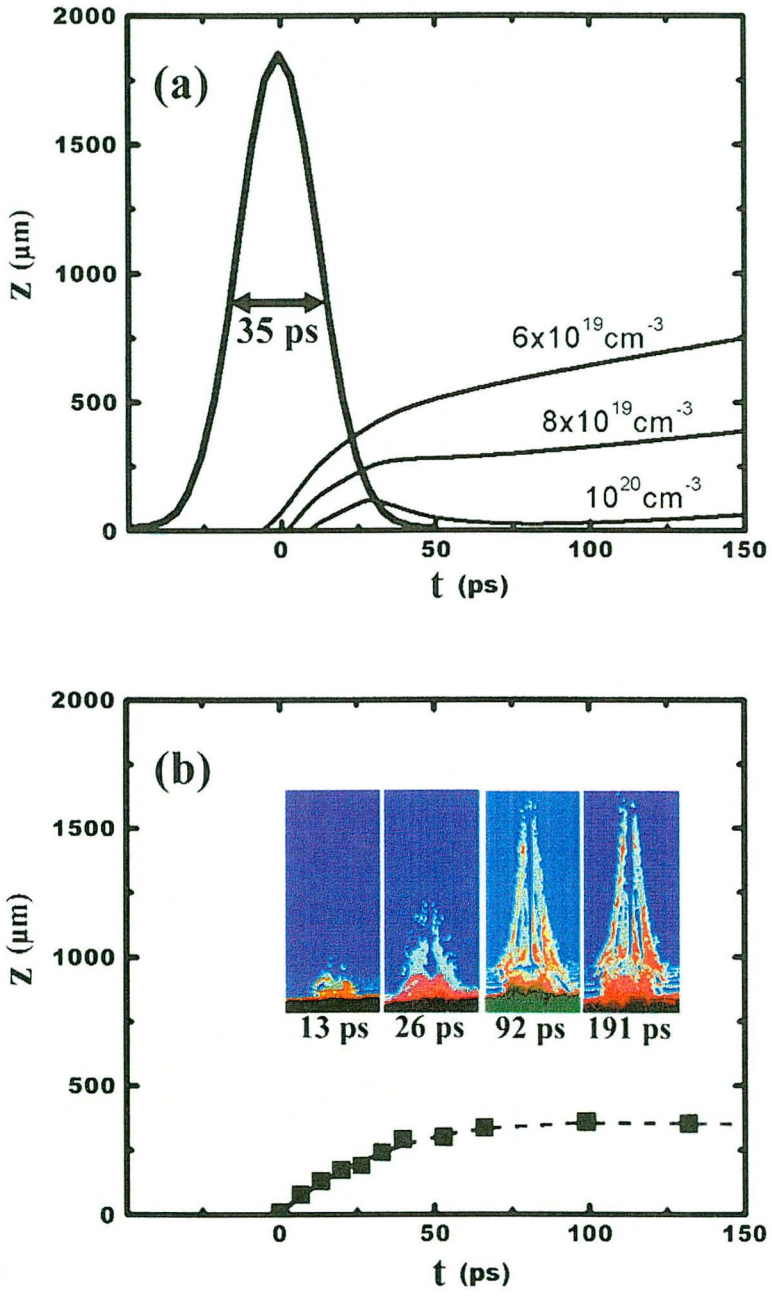

Figure 5.3. (a) Calculated space-time iso-density contours for the electrons inside the plasma. The 35 ps FWHM ablation laser pulse is also shown for arbitrary units. (b) The experimental data for longitudinal plasma extension. The insert shows plasma pictures recorded at four different times. Laser input is from the above.

There are small discrepancies between the calculated results and the measured ones. The calculated longitudinal expansion fronts are slightly greater than the measured ones; experimentally, the plasma also expands in the radial direction whereas only a one-dimensional expansion was considered in the simulation. Despite such discrepancies, there is general agreement between the simulation and the experimental data.

The suppression of the plasma expansion in the longitudinal direction can be attributed to the development of an electric field, E, inside the plasma. One cause of the field is the ejection of energetic electrons from the target surface, which leaves positively charged ions on the target surface. In addition, because ionized gas atoms inside the plasma are much heavier than electrons, they can be considered to be immobile while the electrons expand rapidly away from the target. As a consequence, there is a net positive charge close to the target surface and a negative charge away from the target. The resulting electric field that directs opposite to the incident laser beam acts to suppress further forward movement of the electrons inside the plasma. Figure 5.4 shows a schematic illustration of electric field development above the laser ablated target surface.

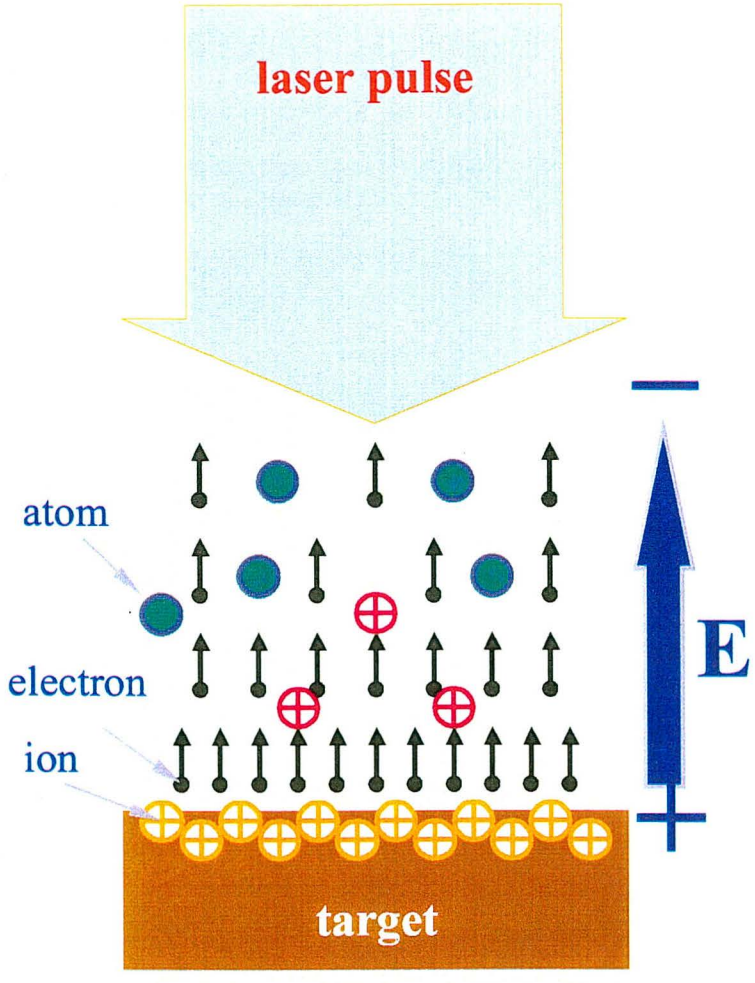

Figure 5.4. A schematic illustration of electric field development inside the plasma.

The calculated space and time development of the electric field above the Cu target is shown in figure 5.5. An electric field as strong as 4 x 10^6 V/m exists above the target.

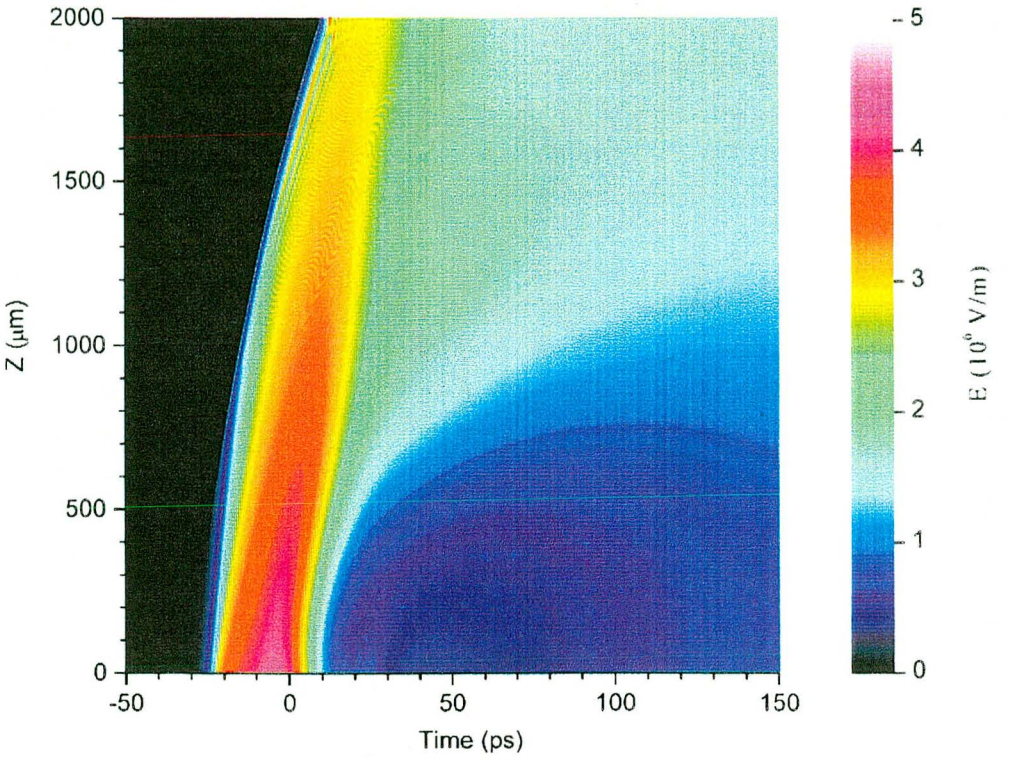

Figure 5.5. Spatial-temporal evolution of the electric field above the laser ablated target.

5.3 Radial expansion of picosecond laser-induced plasma

With a picosecond pulsed laser beam incident on a copper surface, we have observed that an air breakdown plasma forms on the picosecond time scale. This plasma is initiated by the ejection of electrons from the target surface, and it is different from the direct breakdown (Li et al., 1992) of air by the incident laser beam. In this section, we focus on the radial dynamics of the picosecond laser ablation plasma. For fundamental understanding and practical applications, it is instructive to ascertain to what extent the laser ablation plasma absorbs the incident

picosecond laser energy and thereby reduces the efficiency of energy deposition on the target.

Figure 5.6 shows three shadowgraphs of the picosecond laser ablation plasma for delay times of 200, 1000, and 2000 ps. The energy of the laser pulse was fixed at 10 mJ (127 J/cm^2). The longitudinal extent of the air plasma remains approximately constant (Section 5.2) after about 100 ps, and the plasma then expands principally in the lateral (radial) direction. Note that a material plume starts to appear after a few hundred picoseconds; it overlaps with part of the air plasma as it expands.

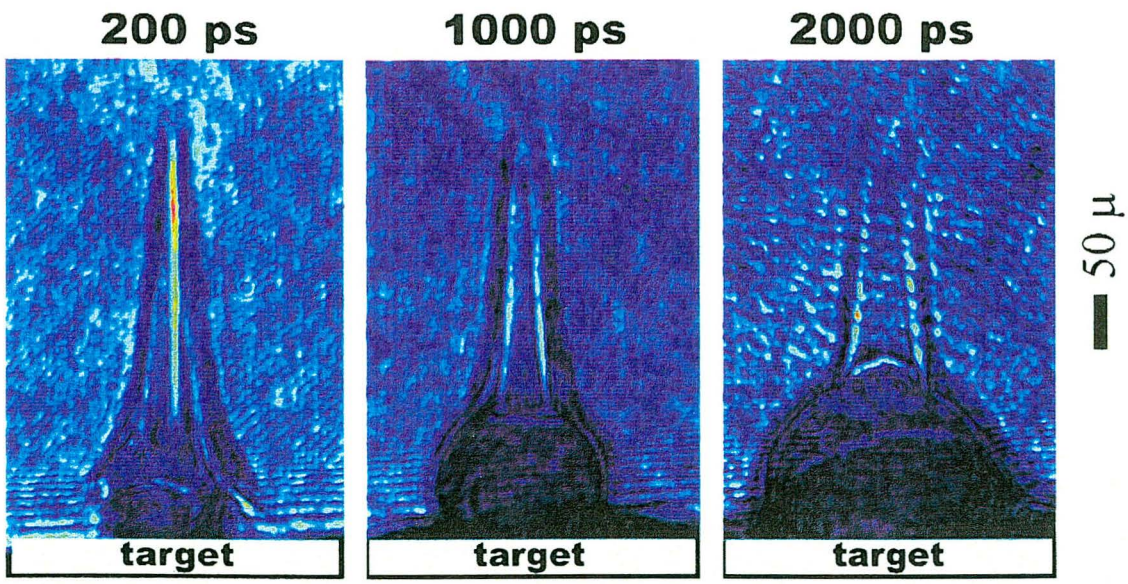

Figure 5.6. Lateral expansion of the picosecond laser ablation plasma taken at 200, 1000, and 2000 ps, respectively. A material vapor plume can be seen to move off the target surface, which overlaps with part of the picosecond plasma near the target.

As determined from both interferometry and simulations, the electron number density of the plasma is on the order of 10^{20} cm^{-3}. At post-pulse times (figure 5.6), the expanding plasma forms an approximate column with a high electron density near the outer radial region and a low density near the incident laser axis (figure 3.10).

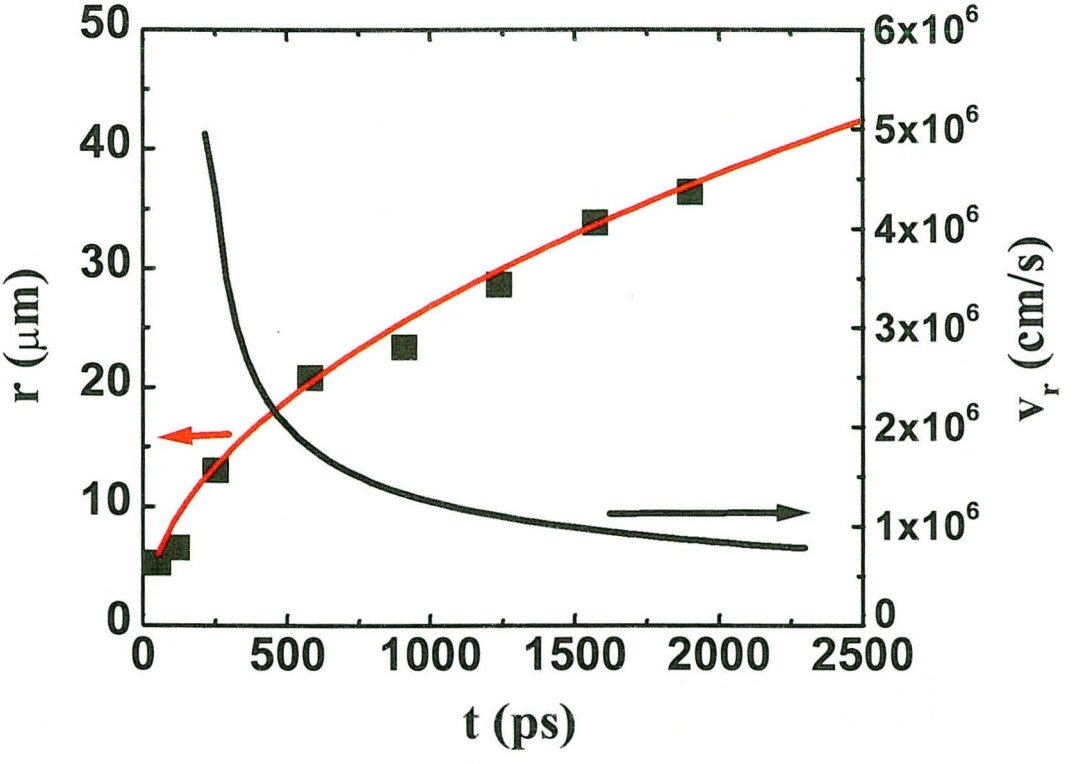

Figure 5.7. Temporal variation of the mean plasma radius and the lateral expansion velocity.

From the interferograms, the radius of the plasma can be determined by measuring the distance between the laser axis and the position at which a shift of interference fringes starts to occur. Measurements from the shadowgraphs yielded similar results for lateral plasma expansion. The temporal variations of the mean plasma radius are shown in figure 5.7; the data were obtained by averaging three sets of measurements from the same plasma picture. The sampling positions were located at approximately 100, 150, and 200 μm above the target surface. The lateral plasma expansion velocities derived from the expansion radius data are also shown in figure 5.7.

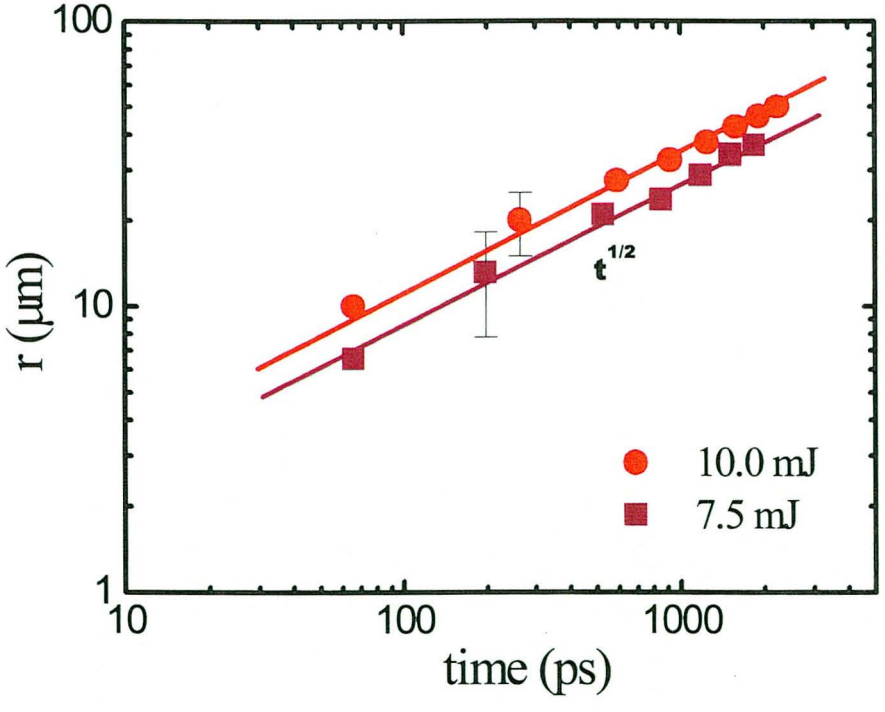

Figure 5.8. Log-log plot of the radius of plasma expansion as a function of time for two incident laser energies at 7.5 mJ and 10.0 mJ.

Figure 5.8 is a plot of the lateral extent (radius) of the plasma as a function of time for two different laser energies, 7.5 and 10.0 mJ. After about 100 ps, the lateral expansion follows the relation, $r \sim t^{1/2}$. This dependence is consistent with the similarity solution for expansion resulting from an instantaneous line source of energy release (Sedov, 1959) As was discussed by Li et al. (1992), the energy driving the radial expansion of the plasma can be estimated using the equation

$$r = C\left(\frac{E_p}{\rho}\right)^{1/4} t^{1/2}$$

Here C is a constant approximately equal to unity, E_p is the energy deposited per unit length which drives the expansion, ρ is the mass density of the air, and t is time. For the experimental conditions of this work, before the 35 ps laser pulse ends, the plasma is gradually heated by the absorption of light from collisional ionization (the inverse Bremsstrahlung process) near the laser axis. The laser spot radius on the target is about 50 μm; it takes about 100 ps for the plasma density and pressure profiles to evolve towards the similarity solution, which assumes an instantaneous release of energy from a line source along the laser axis.

Using the above similarity relation and the experimental data, the energy per unit length, E_p, that drives the lateral expansion of the picosecond laser ablation plasma was calculated to be 8.5 and 18.9 mJ/cm for 7.5 and 10.0 mJ laser pulses, respectively. These results are consistent with the fact that the absorption of laser energy is larger when the air plasma has a larger electron number density corresponding to a higher incident laser energy. Here the peak electron number

density for the 7.5 and 10.0 mJ laser pulses are 4 and 5 x 10^{20} cm^{-3} respectively. For the 10.0 mJ laser pulse, the absorbed energy by the plasma was calculated to be about 10 percent of the overall energy of the 35 ps pulse; for the 7.5 mJ laser pulse, only about 5 percent was absorbed by the plasma to drive its lateral expansion. These measured energies, however, only represent the hydrodynamic component of energy absorption by the air plasma. According to Li et al. (1992), about 20 to 40 percent of the absorbed energy is responsible for the hydrodynamic motion, since a large fraction of the absorbed energy is lost, for example, by line radiation from recombination of ions. As a consequence, the picosecond laser ablation plasma may absorb as much as 50 percent of the overall incident laser energy in the laser fluence range of the present experiment.

Experiments have also been performed to determine the laser fluence dependence of the depth of the craters due to 35 ps, 1064 nm laser ablation of copper in air. A Zygo NewView 200 surface structure analyzing system was employed to measure the crater depth. The system uses scanning white light interferometry to image and measure the micro-structures and topography of target surfaces in three dimensions. Figure 5.9 is a typical ablation crater.

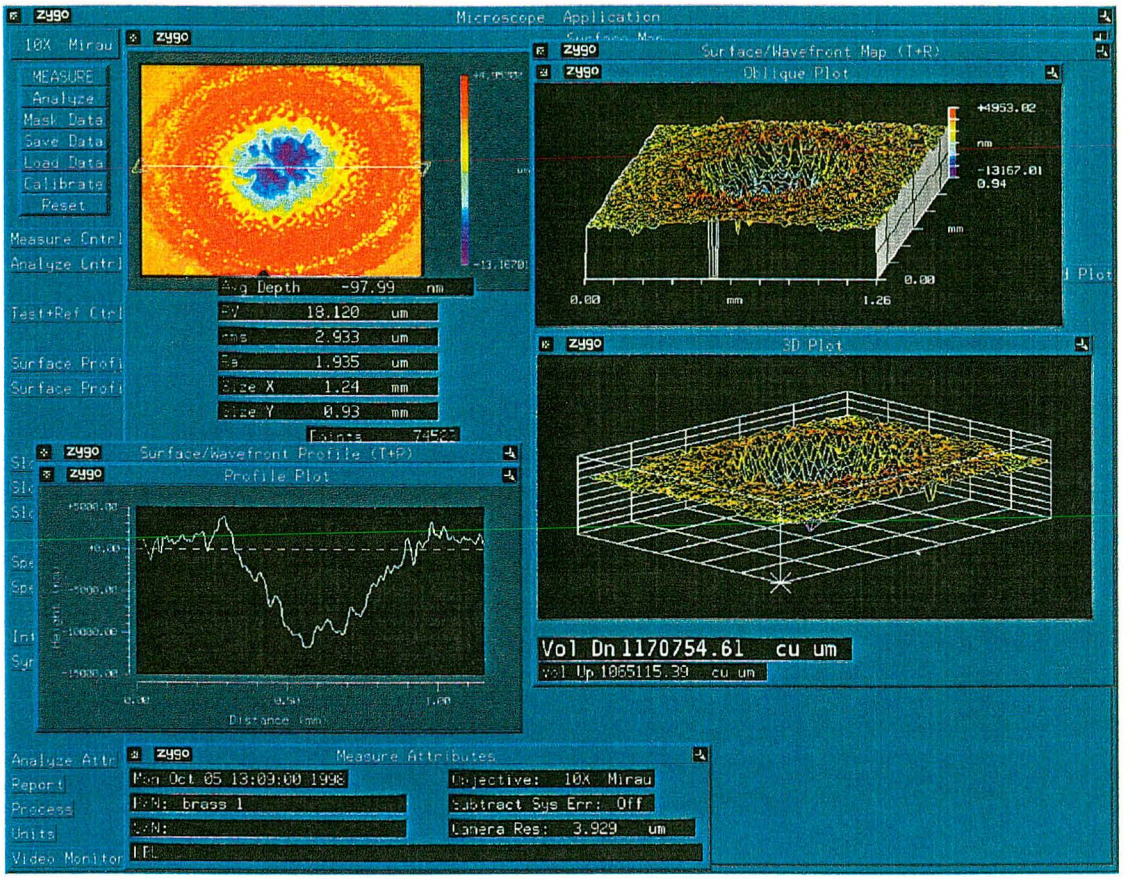

Figure 5.9. A typical laser ablation crater measurement.

The results from the measured crater depth as a function of ablation laser fluence are shown in figure 5.10. As the laser fluence is increased to approximately 80 J/cm^2 (equivalent to a power density of 2 x 10^{12} W/cm^2), the dependence of the crater depth with respect to laser fluence is reduced. This observation implies that the efficiency of deposition of the laser energy into the target material, or laser ablation efficiency, measured by the volume of removed mass per unit laser energy (the slope in figure 5.10), decreases as the laser fluence increases beyond a certain

threshold. Similar observations of a reduced laser ablation efficiency at higher laser fluences have also been reported by other groups (Semerok et al., 1999).

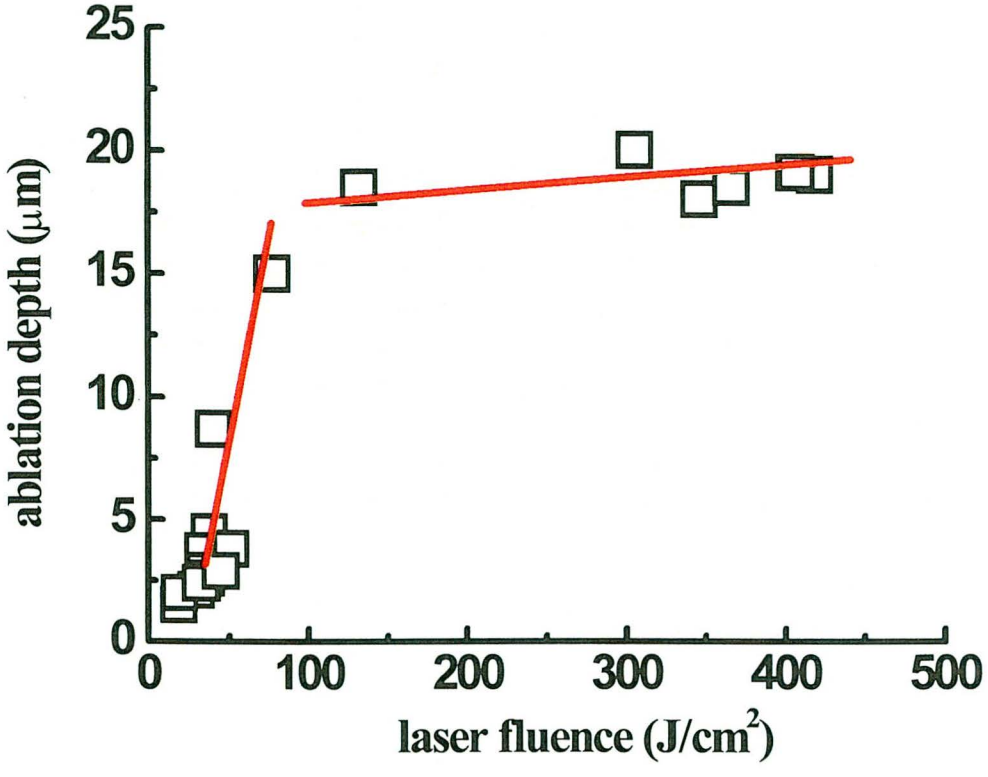

Figure 5.10. Laser fluence dependence of the crater depth for 35 ps, 1064 nm laser ablation of copper.

In fact, we have observed the initiation of the picosecond laser ablation plasma, which appears at a laser power density around 1.5 x 10^{12} W/cm^2. Considering an experimental uncertainty for the laser power density of about 0.5 x 10^{12} W/cm^2, the value of 1.5 x 10^{12} W/cm^2 is consistent with the threshold at which the laser ablation efficiency is reduced. This agreement suggests that the reduced

picosecond laser ablation efficiency results from the formation of the picosecond plasma reported in this work, which may absorb a substantial amount of laser energy as determined from the measurements of the lateral plasma dynamics. The correlation between plasma formation and reduced laser ablation efficiency was not recognized in previous studies for picosecond laser ablation, although in the case of nanosecond laser ablation, the absorption of laser energy by a material vapor plume is apparent (Russo, 1995).

5.4 Summary

In summary, we have studied the longitudinal and lateral expansion of the picosecond laser ablation plasma. The experiments showed that the longitudinal expansion of the plasma was suppressed at post laser times. The significant decrease of longitudinal plasma expansion velocity was reproduced by the simulation. The development of a strong electric field was found to be responsible for the suppression of the longitudinal plasma expansion. After the laser pulse is completed, the lateral expansion radius of the picosecond laser ablation plasma follows a power-law relation, $r \sim t^{1/2}$. A substantial amount of incident laser energy was found to be absorbed by this picosecond plasma.

We have also determined the laser fluence dependence of the ablation crater depth for 35 ps, 1064 nm laser ablation of copper. The experimental results indicate a reduced laser ablation efficiency as the result of the formation of a plasma at the picosecond time scale. Plasma absorption is often undesirable in many applications

involving laser-material interactions. Considering the nature of the picosecond plasma (surface electron emission induced gas ionization), the present experiments imply that plasma absorption during picosecond laser ablation of a solid may be minimized by using either an ambient gas of high ionization energy and/or using low gas pressure.

Chapter 6

CONCLUSIONS AND FUTURE RESEARCH

6.1 Conclusions

As short pulse, high power lasers are finding applications in an increasing number of manufacturing processes, the capability to precisely control the laser energy coupling to target materials becomes more critical. A thorough understanding of the underlying mechanisms during and after high power laser-interaction with materials is important for optimizing practical applications. In this work, we have demonstrated an important feature of picosecond laser ablation, particularly for micro-machining applications. We found that the mass removal efficiency decreases when the ablation laser fluence exceeds a certain threshold. This result suggests that for picosecond laser micro-machining in a gas environment, using very high power laser pulses is less efficient than for lower power pulses. The origin of the reduction of ablation efficiency is the formation of a novel type plasma above the target surface during picosecond laser interactions with the target material.

We have identified the cause of this picosecond plasma from experiments and simulation. Shadowgraph and interferometry experiments indicate that the plasma has an electron number density on the order of 10^{20} cm^{-3}, i.e., an order of magnitude higher than the air density. The initiation of the picosecond plasma was not observed when the air pressure was reduced substantially, or the target material

was removed. Computer simulations based on conservation of particle number, momentum, and energy inside the plasma yielded results consistent with the experimental measurements. A unique boundary condition was employed in the simulation, namely, we allowed laser-induced electron emission from the laser ablated target to provide seed electrons for the initiation of the picosecond plasma. Combined with the experimental and simulation results, we concluded that the formation of the picosecond laser ablation plasma was due to gas breakdown assisted by electron emission from the target surface.

We have further studied the dynamics of the picosecond laser ablation plasma. Both experimental and simulation results indicate that the longitudinal plasma expansion levels off after the ablation laser pulse is ended. We developed a theory to interpret the suppression phenomenon; the development of a strong electric field inside the plasma prevents electrons from further movement away from the target. At post laser times, the expansion of the plasma is primarily in the lateral or radial direction. The radius of the lateral plasma expansion was found to follow a $t^{1/2}$ power law, which is in agreement with the prediction from similarity theory for two-dimensional blast wave development resulting from instantaneous energy release of a line source. By fitting the experimental data to the similarity relation, we concluded that the picosecond laser ablation plasma may absorb a substantial amount of incident laser energy, and thereby shield the target. Considering that the plasma-forming threshold is approximately the same as the threshold for ablation efficiency reduction, we concluded that the origin of the

observed reduction of ablation efficiency is the formation of the picosecond plasma.

In addition to the study of the laser ablation plasma and mass removal efficiency, we have extended the previous investigations of laser-induced electron emission (desorption) from metal surfaces to semiconductors. A model was made based on carrier transport inside the semiconductor material during picosecond laser-semiconductor interactions. We found two distinct regimes for the thermionic electron emission current dependence on laser fluence. The cause of this two-regime feature was identified to be a change in the dominant carrier heating mechanism from interband absorption of laser pulse energy to the Auger recombination of hot carriers inside semiconductors.

For short nanosecond laser induced electron emission from semiconductor surfaces, we demonstrated that nonequilibrium carrier dynamics plays a significant role. For laser energy well below the target melting threshold, we found that for low incident laser fluences, the photoelectric effect dominates electron emission, whereas at higher fluences, thermionic emission resulting from interband absorption is responsible for electron emission. The model results provide a satisfactory interpretation of the measurements.

6.2 Future research

A direct extension of the present experiments would be a parametric study of the formation and dynamics of the picosecond laser ablation plasma. It would be

of great interest to investigate this novel type of plasma under different ambient gas environments with different target materials (e.g., metals, semiconductors, and insulators). A slightly different direction would be a study of laser pulse duration and wavelength influence on the initiation of the laser ablation plasma. No such information, both experimental and theoretical, is available at the present time.

While the experiments presented here are primarily ablation of solids by focusing a laser beam normal to the target surface, it would be of considerable interest to study ablation with the laser beam at a small incident angle. Such an extension would be useful for laser-assisted material processing and micro-machining when laser ablation is combined with other near-field methods (normal incident scheme not convenient). Preliminary experiments at an incident angle of 75 degrees indicate that the picosecond plasma expands along the ablation laser beam, whereas the expansion of the hemispherical material plume is independent of the incident angle of the ablation laser beam.

The one-dimensional computer simulation established in this work can be extended to two- and three-dimensional cases. The magnetic field effect, for instance, which was neglected for one-dimensional model, can therefore be included. We may also extend the present picosecond laser plasma model to include the formation of the material vapor typically a few hundred picoseconds to a nanosecond after the ablation laser pulse. Substantial computing resources would be needed for these analyses.

The experimental and theoretical work presented here should be important for practical applications such as ultrafast laser micro-machining. It would be very useful to identify material-specific laser and gas conditions for maximizing the ablation efficiency. Another application would be in the plasma itself, a plasma with high electron number density may be a valuable source for X-ray generation. A well-controlled X-ray pulse would have many applications ranging from material characterization to medical diagnosis.

References:

R. R, Alfano, ed., *Semiconductors probed by ultrafast laser spectroscopy* (Academic, New York, 1984).

S. I. Anisimov, B. L. Kapeliovich, and T. L. Perelman, Sov. Phys. - JETP, **39**, 375 (1974).

S. I. Anisimov, B. S. Luk'yanchuk, and A. Luches, Appl. Surf. Sci., **96**, 24 (1996).

J. H. Bechtel, W. L. Smith, and N. Bloembergen, Phys. Rev. B, **15**, 4557 (1977).

M. Bensoussan and J. M. Moison, J. de Phys., **C7**, 149 (1981).

M. Bensoussan, J. M. Moison, B. Stoesz, and C. Sebenne, Phys. Rev. B, **23**, 992 (1981).

J. Bokor, Science, **246**, 1130 (1989).

I. W. Boyd, S. C. Moss, T. F. Boggess, and A. L. Smirl, Appl. Phys. Lett., **45**, 80 (1984).

G. Callies, P. Berger, and H. Hugel, J. Phys. D, **28**, 794 (1995).

K. R. Chen, J. N. Leboeuf, R. F. Wood, D. B. Geohegan, J. M. Donato, C. L. Liu, and A. A. Puretzky, Phys. Rev. Lett., **75**, 4706 (1995).

T. R. Clark and H. M. Milchberg, Phys. Rev. Lett., **78**, 2373 (1997).

B. Craig, Laser Focus World, **34**, 79 (1998).

M. Deutsch and I. Beniaminy, J. Appl. Phys., **54**, 137 (1983).

J. T. Dickinson, Nucl. Instrum. Meth. B, **91**, 634 (1994).

D. Dijkkamp, T. Venkatesan, X. D. Wu, S. A. Shaheen, N. Juswari, Y. H. Min-Yee, W. L. McLean, and M. Croft, Appl. Phys. Lett., **51**, 619 (1987).

E. Fogarassy and S. Lazare, eds., *Laser Ablation of Electronic Materials* (North-Holland, Amsterdam, 1992).

M. I. Gallant and H. M. van Driel, Phys. Rev. B, **26**, 2133 (1982).

D. B. Geohegan, A. A. Puretzky, G. Duscher, and S. J. Pennycook, Appl. Phys. Lett., **73**, 438 (1998).

C. P. Grigoropoulos, in *Laser Ablation and Desorption*, eds., J. C. Miller and R. F. Haglund (Academic, New York, 1998).

R. F. Haglund, Jr., Appl. Surf. Sci., **98**, 1 (1996).

C. Herring and M. H. Nichols, Rev. Mod. Phys., **21**, 185 (1949).

J. R. Ho, C. P. Grigoropoulos, and J. A. C. Humphrey, J. Appl. Phys., **78**, 4696 (1995).

H. Hora, *Plasmas at high temperature and density* (Springer, New York, 1991).

F. P. Incropera and D.P. DeWitt, *Fundamentals of heat and mass transfer*, 4th ed. (Wiley, New York, 1996).

F. C. Jahoda and G. A. Sawyer, in *Method of experimental physics*, Vol. 9, Part B, eds., R. H. Lovberg and H. R. Greim (Academic, New York, 1971).

C. Kittel, *Introduction to solid state physics*, 7th ed. (Wiley, New York, 1996).

G. T. A. Kovacs, N. I. Maluf, and K. E. Petersen, Proc. IEEE, **86**, 1536 (1998).

W. L. Kruer, *The physics of laser plasma interactions* (Addison-Wesley, Redwood City, CA, 1988).

Landolt-Bornstein, *numerical data and functional relationships in science and technology*, vol.17 and vol.22 (Springer, New York, 1982).

R. J. LeVeque, *Numerical methods for conservation laws*, 2nd ed. (Birkhäuser, Boston, 1992).

Y. M. Li, J. N. Broughton, R. Fedosejevs, and T. Tomie, Optics Comm., **93**, 366 (1992).

C. P. Lin, M. W. Kelly, S. A. B. Sibayan, M. A. Latina, and R. R. Anderson, IEEE J. Selected Topics in Quantum Electronics, **5**, 963 (1999).

L. A. Lompre, J. M. Liu, H. Kurz, and N. Bloembergen, Appl. Phys. Lett., **44**, 3 (1984).

D. H. Lowndes, D. B. Geohegan, A. A. Puretzky, D. P. Norton, and C. M. Rouleau, Science, **273**, 898 (1996).

M. Lundstrom, *Fundamentals of Carrier Transport* (Addison-Wesley, Reading, 1990).

S. S. Mao, X. L. Mao, R. Greif, and R. E. Russo, Appl. Surf. Sci., **129**, 206 (1998).

X. L. Mao, W. T. Chan, M. A. Shannon, and R. E. Russo, J. Appl. Phys., **74**, 4915 (1993).

X. L. Mao and R. E. Russo, Appl. Phys. A, **64**, 1 (1997).

J. C. Miller, ed., *Laser Ablation: Principles and Applications* (Springer, New York, 1994).

J. C. Miller and R. F. Haglund, Jr., eds., *Laser Ablation and Desorption* (Academic, New York, 1998).

A. M. Morales and C. M. Lieber, Science, **279**, 208, 1998.

M. M. Murnane, H. C. Kapteyn, M. D. Rosen, and R. W. Falcone, Science, **251**, 531 (1991).

K. A. Nugent, Appl. Optics, **24**, 3101 (1985).

T. W. Odom, J. L. Huang, P. Kim, and C. M. Lieber, Nature, **391**, 62 (1998).

G. Petite, P. Agostini, R. Trainham, E. Mevel, and P. Martin, Phys. Rev. B, **45**, 12210 (1992).

T. Q. Qiu and C. L. Tien, J. Heat Trans., **115**, 835 (1993).

J. F. Ready, *Effects of high power laser radiation* (Academic, New York, 1971).

D. Ress, L. B. DaSilva, P. A. London, J. E. Trebes, S. Mrowka, R. J. Procassini, T. W. Barbee, Jr., and D. E. Lehr, Science, **265**, 514 (1994).

R. E. Russo, Applied Spectroscopy, **49**, 14 (1995).

R. E. Russo, D. B. Geohegan, R. F. Haglund, and K. Murakami, eds., *Laser Ablation* (Elsevier, Amsterdam, 1998).

R. E. Russo and X. L. Mao, in *Laser ablation and desorption*, eds., J. C. Miller and R. F. Haglund (Academic, New York, 1998) .

L. I. Sedov, *Similarity and Dimensional Methods in Mechanics* (Academic, New York, 1959).

A. Semerok, C. Chaleard, V. Detalle, J.-L. Lacour, P. Maushien, P. Meynadier, C. Nouvellon, B. Salle, P. Palianov, M. Perdrix, and G. Petite, Appl. Surf. Sci., **139**, 311 (1999).

W. J. Siekhaus, J. H. Kinney, D.Milam, and L. L. Chase, Appl. Phys. A, **39**, 163 (1986).

L. Spitzer, Jr., *Physics of fully ionized gases* (Interscience, New York, 1956).

P. G. Strupp, P. C. Stair, and E. Weitz, J. Appl. Phys., **69**, 3472 (1991).

M. Tabak, J. Hammer, M. E. Glinsky, W. L. Kruer, S. C. Wilks, J. Woodworth, E. M. Campbell, M. D. Perry, and R. J. Mason, Phys. Plasmas, **1**, 1626 (1994).

J C. Tannehill, D A. Anderson, and R. H. Pletcher, *Computational fluid mechanics and heat transfer*, 2nd ed. (Taylor & Francis, Washington DC, 1997).

H. M. van Driel, , Phys. Rev. B, **35**, 8166 (1987).

M. von Allmen and A. Blatter, *Laser-beam interactions with materials: physical principles and applications*, 2nd ed. (Springer, New York, 1995).

R. F. Wood, K. R. Chen, J. N. Leboeuf, A. A. Puretzky, D. B. Geohegan, Phys. Rev. Lett., **79**, 1571 (1997).

X. D. Wu, D. Dijkkamp, S. B. Ogale, A. Inam, E. W. Chase, P. F. Miceli, C. C. Chang, J. M. Tarascon, and T. Venkatesan, Appl. Phys. Lett., **51**, 861 (1987).

A. Yariv, *Optical electronics in modern communications*, 5th ed. (Oxford University Press, New York, 1997).

P. E. Young, H. A. Baldis, R. P. Drake, E. M. Cambell, and K. G. Estabrook, Phys. Rev. Lett., **61**, 2336 (1988).

Ernest Orlando Lawrence Berkeley National Laboratory
One Cyclotron Road | Berkeley, California 94720

Prepared for the U.S. Department of Energy under Contract No. DE-AC03-76SF00098